

A joint MeerKAT and Parkes view of Omega Centauri: New TRAPUM Searches and Pulsar Timing

Miquel Colom i Bernadich^{1,2}, Shi Dai^{3,4}, Federico Abbate¹, Matthew Kerr⁵, Matteo Bachetti¹, Yash Bhargava¹, Sarah Buchner⁶, Simon Johnston³, Marta Burgay¹, Andrea Possenti¹, Rouhin Nag^{1,7}, Alessandro Ridolfi⁸, Amodio Carleo¹, Alessandro Corongiu¹, Paulo C. C. Freire², Fernando Camilo⁶, Weiwei Chen², Mario Cadelano^{9,10}, Dhanraj Risbud^{2,8}, Prajwal V. Padmanabh^{11,12}, David J. Champion², Michael Kramer², Benjamin Stappers¹⁷, Maciej Serylak¹³, Vishnu Balakrishnan¹⁴, Matthew Bailes^{15,16}, Arunima Dutta², Laila Vleeschower^{17,18}, Vivek Venkatraman Krishnan², and Yunpeng Men²

¹ INAF – Osservatorio Astronomico di Cagliari, via della Scienza 5, 09047 Selargius (CA), Italy

² Max-Planck-Institut für Radioastronomie, Auf dem Hügel 69, D-53121 Bonn, Germany

e-mail: miquel.colomibernadich@inaf.it, mcbernadich@mpi-fr-bonn.mpg.de

³ Australia Telescope National Facility, CSIRO, Space and Astronomy, PO Box 76, Epping NSW 1710, Australia

⁴ School of Science, Western Sydney University, Locked Bag 1797, Penrith, NSW 2751, Australia

⁵ Space Science Division, Naval Research Laboratory, Washington, DC 20375–5352, USA

⁶ South African Radio Astronomy Observatory, Liesbeek House, River Park, Cape Town 7705, South Africa

⁷ University of Cagliari, Monserrato University Campus - SP Monserrato-Sestu Km 0,700 - 09042 Monserrato (CA), Italy

⁸ Fakultät für Physik, Universität Bielefeld, Postfach 100131, D-33501 Bielefeld, Germany

⁹ Department of Physics and Astronomy ‘Augusto Righi’, University of Bologna, via Gobetti 93/2, I-40129 Bologna, Italy

¹⁰ INAF – Astrophysics and Space Science Observatory of Bologna, via Gobetti 93/3, I-40129 Bologna, Italy

¹¹ Max Planck Institute for Gravitational Physics (Albert Einstein Institute), D-30167 Hannover, Germany

¹² Leibniz Universität Hannover, D-30167 Hannover, Germany

¹³ SKA Observatory, Jodrell Bank, Lower Withington, Macclesfield, Cheshire, SK11 9FT, UK

¹⁴ Center for Astrophysics, Harvard & Smithsonian, Cambridge, MA 02138-1516, USA

¹⁵ Centre for Astrophysics and Supercomputing, Swinburne University of Technology, PO Box 218, Hawthorn, VIC 3122, Australia

¹⁶ OzGrav: The ARC Centre of Excellence for Gravitational Wave Discovery, Hawthorn, VIC 3122, Australia

¹⁷ Jodrell Bank Centre for Astrophysics, Dept. of Physics & Astronomy, The University of Manchester, Manchester M13 9PL, UK

¹⁸ Center for Gravitation, Cosmology, & Astrophysics, Dept. of Phys., Univ. of Wisconsin-Milwaukee, Milwaukee, WI 53201, USA

Received September 30, 20XX

ABSTRACT

Context. Millisecond pulsars (MSPs) are powerful probes of globular clusters (GCs), tracing stellar evolution, cluster dynamics, and the local gravitational potential.

Aims. We search for new MSPs in the GC Omega Centauri, derive updated timing solutions for its known pulsar population, and investigate the high-energy emission, cluster potential, and MSP demographics.

Methods. We perform Fourier-domain acceleration and jerk searches on MeerKAT observations, and carry out pulsar timing using MeerKAT and Parkes Murriyang data spanning 2021–2025. We fold *Fermi* LAT and NICER photons using updated radio ephemerides to search for high-energy pulsations.

Results. We discover a new isolated MSP, PSR J1326–4728S (hereafter S), with a spin period of 4.538 ms and a dispersion measure of $96.24 \text{ cm}^{-3} \text{ pc}$. We update the orbital parameters of all known binary systems, with those of I, N, and Q differing significantly from previous estimates, and obtain new timing solutions for G, H, and K. Pulsars B, G, H, K, and L exhibit black widow-like properties, I, N and Q are found in wider binaries, with N and Q having $> 0.2 M_{\odot}$ companions, and N showing a significant orbital eccentricity ($e = 0.093$). Significant spin period derivatives are measured for eight pulsars and interpreted as arising from the cluster gravitational potential. No pulsed high-energy emission is detected from individual pulsars.

Conclusions. The inferred line-of-sight accelerations are consistent with a King-model gravitational potential. While our measurements are insensitive to an intermediate-mass black hole with mass 10^3 – $10^4 M_{\odot}$, they place an upper limit of $< 10^5 M_{\odot}$ at 90% confidence. The high fraction of isolated MSPs and black widows systems, and possibly the eccentricity of N, are difficult to reconcile with MSP population predictions based solely on encounter rates. Instead, these properties likely reflect the complex evolutionary history of Omega Centauri, with part of its MSP population having formed in denser environments than observed today.

Key words. Globular clusters - Omega Centauri – pulsars – binaries – kinematics and dynamics

1. Introduction

Omega Centauri (ω Cen, also NGC 5139) is a unique globular cluster (GC). With a mass of $3.55 \times 10^6 M_{\odot}$ and a core ra-

dius of 4.30 pc (Baumgardt & Hilker 2018), it is the largest and most massive GC in the Milky Way. It follows a retrograde orbit (Dinescu et al. 1999) and exhibits exceptional stellar complexity, including spatially mixed metallicity populations (Nitschai et al.

Table 1: The nineteen currently known pulsars in ω Cen and their properties, showing the discovery reference, the angular separation from the cluster centre, θ , the spin period, P_s , the spin period derivative \dot{P}_s , the dispersion measure, DM, the orbital period, P_b , the orbital eccentricity, e , and the minimum companion mass, M_c

PSR	Discovery	θ '	P_s ms	\dot{P}_s $10^{-20} \text{ s s}^{-1}$	DM $\text{cm}^{-3} \text{ pc}$	P_b days	x ls	e	M_c M_\odot
A	Dai et al. (2020)	1.93	4.109	2.73	100.33			isolated	
B	Dai et al. (2020)	0.76	4.792	-5.43	100.28	0.0896	0.0215	$\lesssim 10^{-4}$	> 0.013
C	Dai et al. (2020)	1.98	6.868	1.01	100.66			isolated	
D	Dai et al. (2020)	2.50	4.579	-4.12	96.55			isolated	
E	Dai et al. (2020)	1.58	4.208	1.63	94.34			isolated	
F	Chen et al. (2023)	~ 1.0	2.273	...	98.29			isolated	
G	Chen et al. (2023)	1.96	3.304	2.77	99.75	0.1086	0.0322	$\lesssim 10^{-4}$	> 0.018
H	Chen et al. (2023)	0.56	2.520	3.99	98.17	0.1357	0.0219	$\lesssim 10^{-4}$	> 0.010
I	Chen et al. (2023)	~ 3.53	18.95	...	102.56	3.5083	0.7852	$\lesssim 10^{-3}$	> 0.043
J	Chen et al. (2023)	~ 1.80	3.686	...	97.28			isolated	
K	Chen et al. (2023)	1.89	4.716	-0.91	94.78	0.0939	0.0680	$\lesssim 10^{-4}$	> 0.042
L	Chen et al. (2023)	~ 3.32	3.537	...	101.48	0.1589	0.0618	$\lesssim 10^{-4}$	> 0.027
M	Chen et al. (2023)	~ 2.4	4.604	...	101.47			isolated	
N	Chen et al. (2023)	~ 2.66	6.884	...	102.1	6.3566	5.7231	0.0928	> 0.232
O	Chen et al. (2023)	~ 1.5	6.160	...	94.305			isolated	
P	Chen et al. (2023)	~ 1.0	2.795	...	102.17			isolated	
Q	Chen et al. (2023)	~ 2.3	4.130	...	95.955	1.5400	1.9938	$\lesssim 10^{-4}$	> 0.205
R	Chen et al. (2023)	~ 3.9	10.29	...	102.2			isolated	
S	this work	~ 2.32	4.538	...	96.24			isolated	

Notes. θ assumes RAJ, DECJ = $13^{\text{h}}26^{\text{m}}47.24^{\text{s}}$, $-47:28:46.5$ for the cluster (Harris 2010). Pulsar positions not reported in this work are taken from Chen et al. (2023). Minimum companion mass (M_c) is derived from the mass function (pulsar mass $M_p = 1.35 M_\odot$, inclination angle $i = 90^\circ$).

2024), up to 15 distinct main-sequence populations (Bellini et al. 2017), and possibly a wide stellar age spread of 10-13 Gyr (Villanova et al. 2014; Tailo et al. 2016; Clontz et al. 2024).

Owing to these properties, ω Cen is considered the stripped nuclear cluster of a dwarf galaxy accreted by the Milky Way (Lee et al. 1999; Hilker & Richtler 2000; Bekki & Freeman 2003; Pagnini et al. 2025), linked to the Sequoia (Myeong et al. 2019) or Gaia-Enceladus (Massari et al. 2019; Pfeffer et al. 2021; Limberg et al. 2022) mergers, and Galactic halo tidal stellar streams (Majewski et al. 2012; Ibata et al. 2019).

There is ongoing debate regarding the presence of a central intermediate-mass black hole (IMBH) of 10^3 – $10^4 M_\odot$ in ω Cen. Some studies support its existence from stellar kinematics (Noyola et al. 2008, 2010; Jalali et al. 2012; Baumgardt 2017; Häberle et al. 2024), while others place stringent upper limits on its mass (van der Marel & Anderson 2010; Bañares-Hernández et al. 2025) or instead favour an extended central cluster (Zocchi et al. 2017, 2019; Evans et al. 2022; Bañares-Hernández et al. 2025).

Here, we investigate the pulsar population of ω Cen (see Table 1 for a complete list) with MeerKAT¹ and Parkes². Pulsars are powerful probes of GC environments due to their timing stability and sensitivity to cluster properties. Measurements of spin period derivatives constrain the cluster acceleration field and thus its mass distribution (e.g. Prager et al. 2017; Freire et al. 2017). MSP populations also trace stellar dynamics, with total and isolated populations possibly correlating with the total stellar encounter rate (Verbunt & Hut 1987; Hui et al. 2010; Bahramian et al. 2013), and the encounter rate per binary (Verbunt & Freire 2014; Rasio & Heggge 1995). Finally,

MSP populations are linked to the global γ -ray emission of GCs (de Menezes et al. 2019), with γ -ray pulsations being detectable after folding with radio timing solutions (e.g. Freire et al. 2011).

All of these aspects are relevant for ω Cen. Prior to this work, timing solutions were available only for PSR J1326–4728A to E, (hereafter A–E, Dai et al. 2023). Measurements of the spin-period derivatives (\dot{P}_s) were used to place initial constraints on the cluster acceleration field, showing broad consistency with the GC density profile and potential presented by King (1962). Possible exceptions were B and D, whose inferred line-of-sight (LOS) accelerations marginally exceeded the expected limits.

Furthermore, ω Cen hosts a majority of isolated pulsars, posing a challenge to our understanding of the formation of its pulsar population. Isolated MSPs in GCs are thought to arise from binary disruptions during stellar encounters (Verbunt & Freire 2014). However, as discussed in Chen et al. (2023), this interpretation is problematic for ω Cen given its low encounter rate per system. By contrast, GCs with much higher encounter rates per binary are instead dominated by isolated MSPs.

Finally, the cluster overlaps with γ -ray source of $L_\gamma = 3.6 \pm 0.3 \times 10^{34} \text{ erg s}^{-1}$, consistent with a population of 20 to 30 MSPs (Abdo et al. 2010; de Menezes et al. 2019). Dai et al. (2023) searched for γ -ray pulsations using the timing solutions of A–E, but without success. The non-detection was interpreted as the γ -ray emission being distributed over the collective population. However, new discoveries provide a renewed opportunity for γ -ray pulsation searches. Alternatively, it has been postulated that the γ -ray emission originates from dark matter annihilation (Brown et al. 2019; Reynoso-Cordova et al. 2021).

In this paper, we address these topics with new pulsar searches and timing analyses. Section 2 describes the Parkes and MeerKAT data set used in this work. In Section 3, we present new pulsar searches in MeerKAT observations and the discov-

¹ <https://www.sarao.ac.za/science/meerkat/>

² <https://www.parkes.atnf.csiro.au/>

ery of pulsar S. Section 4 details the derivation of updated timing solutions for A–E, new timing solutions for G, H, and K, and orbital solutions for I, L, N, and Q. Section 5 presents searches for γ -ray and X-ray pulsations using *Fermi* LAT, NICER, and XMM-Newton observations. Finally, in Section 6, we discuss the implications of our results, including dynamical constraints on the potential of ω Cen, a discussion of compatibility with a central IMBH, and an assessment of the pulsar population in the context of the cluster’s encounter rates.

2. Observations included in this study

2.1. Parkes observations

Parkes observations with the Ultra Wideband Low-frequency (UWL; Hobbs et al. 2020) receiver of the Murriyang telescope (704–4032 MHz) were obtained as part of the long-term P1041 observing project, dedicated to the follow-up of pulsars in this GC. In this study, we included all observations carried out between 1 April 2020 and 20 May 2025, performed at approximately monthly cadence with a break between February 2024 and April 2025. Individual observing sessions lasted between three and five hours, providing good pulse integration and a total of approximately 160 hours of observing time.

Observations were recorded in search-mode with the MEDUSA backend (Hobbs et al. 2020) with 3328 full-Stokes resolution, 1 MHz channels coherently de-dispersed at $DM = 99 \text{ cm}^{-3} \text{ pc}$, and with 64 μs sampling. In addition, prior to the main observations, Murriyang also recorded 3-min long observations of noise diodes for polarisation calibration.

2.2. MeerKAT observations

MeerKAT data were collected on multiple observing sessions within 2021–2025 as part of the Transients and Pulsars with MeerKAT (TRAPUM³, Stappers & Kramer 2016) and MeerTIME⁴ (Bailes et al. 2020) projects. Our analysis included data from eight observations from all available MeerKAT receivers: L-band (856–1712 MHz), S-band (S1: 1968–2843 MHz, Barr 2018), and Ultra-High Frequency (UHF, 544–1088 MHz).

These observations were beamformed by the Filterbanking Beamformer User Supplied Equipment (FBFUSE), and were subsequently stored as search-mode filterbanks (without coherent de-dispersion) in the Accelerated Pulsar Search User Supplied Equipment (APSUSE, see Barr 2018; Padmanabh et al. 2023). Some observations implemented a full coherent beam tiling derived with MOSAIC⁵ (Chen et al. 2021), with additional coherent beams synthesised on optimal pulsar and ATCA source positions as reported by Dai et al. (2023) and Chen et al. (2023) (see Table A.1 in Appendix A for a more detailed listing).

Additional MeerKAT observations were obtained under the MeerTIME programme using the Pulsar Timing User Supplied Equipment (PTUSE) backend (Bailes et al. 2020) to investigate the eclipsing pun upcoming publication, in this work we used the 14 February 2024 L-band observation of pulsar L to constrain its orbital parameters.

3. New searches on TRAPUM data

3.1. Aims

We used the APSUSE data to search for new pulsars. The objectives were (i) to perform a deep search of the 12 coherent beams assigned to ATCA-imaged sources reported by Dai et al. (2023), and (ii) to find new pulsars in a 3-hour-lo UHF observation.

The search of the ATCA beams was performed on the 21 April 2021 L-band observation. An exhaustive search at $10 \mu\text{Jy}$ sensitivity of the MOSAIC coherent beam tiling of this dataset was previously carried out by Chen et al. (2023), resulting in the discovery of 13 new pulsars. We complemented this work by searching the beams centred on the ATCA radio sources.

The search on the 11 February 2025 UHF observation mirrored the L-band one presented by Chen et al. (2023), but it targeted pulsars with potentially steep spectral indices. Our search reached a sensitivity of $20 \mu\text{Jy}$, estimated with the radiometer equation (Dewey et al. 1985) and the MeerKAT specifications⁶ (details in Appendix B).

3.2. Implementation

We implemented Fourier-domain jerk (Andersen & Ransom 2018) and GPU-accelerated acceleration searches (Ransom et al. 2002) on individual beams with PRESTO⁷. The searches were run with PULSAR_MINER⁸, a PRESTO-based searching pipeline (Ridolfi et al. 2021). The filterbanks were sub-banded at $DM = 99 \text{ cm}^{-3} \text{ pc}$, resulting in 128 frequency channels for the ATCA search, and 256 for the UHF. The time resolutions were $153.1 \mu\text{s}$ and $120.5 \mu\text{s}$. Radio-frequency interference (RFI) was excised using PRESTO’s `rfind`, masking 10–15% of frequency channels.

We adopted a DM search range of $90\text{--}110 \text{ cm}^{-3} \text{ pc}$, based on the DM of previously known pulsars. For the acceleration searches, we assumed a maximum Fourier-frequency derivative of $z_{\text{max}} = 200$, and allowed the summing of up to eight harmonics. For the jerk searches, we limited the Fourier-frequency derivatives to $z_{\text{max}} = 100$ and $w_{\text{max}} = 300$, respectively, and restricted the harmonic summing to four (see Andersen & Ransom 2018 for the definition of these parameters). We also imposed a minimum FFT significance threshold of 3 for folding.

Finally, to account for pulsars with extreme accelerations or jerks, we implemented segmented searches in addition to searches on the entire observations. The 4-hour files from the ATCA beams were segmented into chunks of 10, 30, 60, and 120 minutes, while the 3-hour files from the UHF observation were divided into segments of 10, 20, 45, and 90 minutes.

The beams included in these searches are shown in the sky map presented in Fig. B.1 in Appendix B. The search on ATCA beams is complete and yielded no new pulsars with flux densities above $10 \mu\text{Jy}$ at L-band.

3.3. UHF discovery: PSR J1326–4728S

Pulsar S was discovered in beam `cfbf00035` from the 11 February 2025 UHF observation, achieving a signal-to-noise ratio of ~ 18 in the full integration. It exhibited a barycentric spin period of $P_s = 4.537782062(58) \text{ ms}$ at a dispersion measure of $DM = 96.240 \text{ cm}^{-3} \text{ pc}$, with no evidence for significant accel-

³ <https://www.trapum.org/>

⁴ <http://www.meertime.org/>

⁵ <https://github.com/wchenastro/mosaic>

⁶ <https://skafrica.atlassian.net/wiki/spaces/ESDKB/pages/277315585/MeerKAT+specifications>

⁷ https://github.com/jintaolu/presto2_on_gpu

⁸ https://github.com/alex88ridolfi/PULSAR_MINER

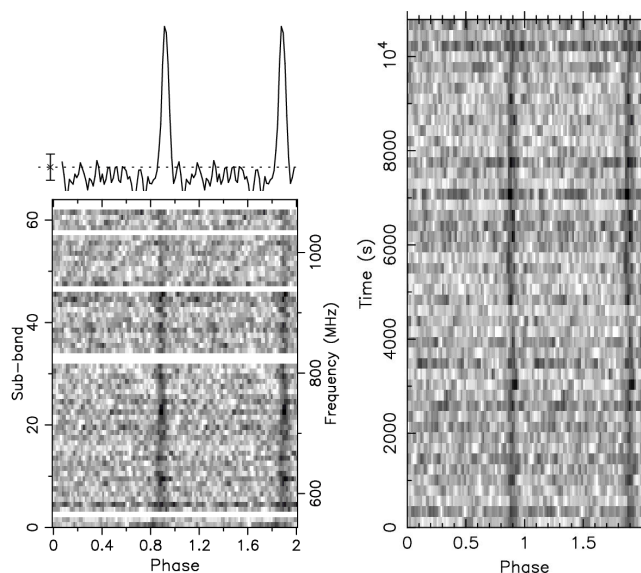


Fig. 1: prepfold diagnostic plots from 11 February 2025, showing the detection of pulsar S in the three-hour integration. Top left: integrated pulse profile. Bottom left: frequency–phase greyscale. Right: time–phase greyscale.

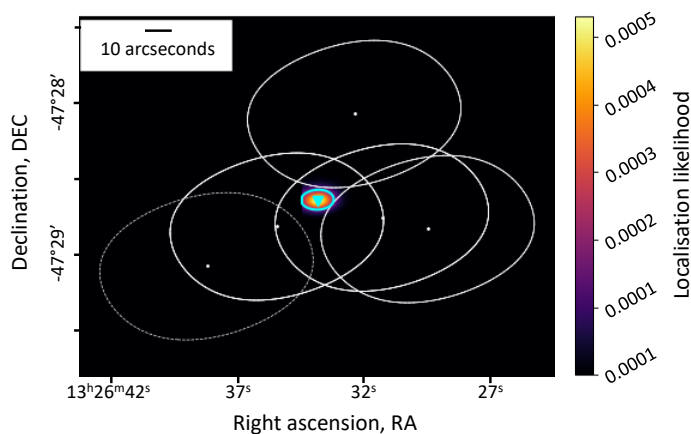


Fig. 2: SeeKAT localisation map of pulsar S, obtained from detections in multiple neighbouring beams.

eration or jerk. Its integrated pulse profile, together with the frequency– and time–phase diagrams, is shown in Figure 1.

Significant re-detections were achieved through direct re-folding of two neighbouring MOSAIC tiling beams, as well as the beams dedicated to pulsar D and ATCA source 7 from Dai et al. (2020) due to their proximity, resulting in a total of five significant detections (see Figure 2). We used SeeKAT⁹ to perform a χ^2 localisation of S based on the beam shapes, beam positions, and detection signal-to-noise ratios (Bezuidenhout et al. 2023). The localisation, shown in Figure 2, yielded a refined position of RAJ, DECJ = $13^{\text{h}}26^{\text{m}}33.76(1)^{\text{s}}$, $-47^{\circ}28:38.50 \pm 1.5$.

With the localised position, we folded the closest beams from the L-band observations obtained on 21 and 27 March 2021. No single beam was clearly optimal, as the source lays close to the edges of all neighbouring beams. The resulting re-folded detections yielded a prepfold significance of ~ 6 over the full integration time, explaining why this pulsar was missed

in Chen et al. (2023). No change in the spin period was observed, indicating that pulsar S is likely not in binary.

4. Timing analysis

4.1. Phase-coherent timing solutions

We updated the phase-coherent timing solutions for A, B, C, D, and E, and derived new ones for G, H, and K. The solutions were obtained by fitting times of arrivals (ToAs) derived from MeerKAT and Murriyang observations. As priors, we used the timing solutions provided in Dai et al. (2023), and the orbital solutions and phase-connected solutions derived with our custom orbital fitting software¹⁰ and dracula¹¹ (see Appendix C).

We folded the optimal MeerKAT filterbanks and the Murriyang search-mode data using dspsr¹² (van Straten & Bailes 2011), and excised them of RFI with c1fd (an outlier-detection algorithm, Morello et al. 2019). We processed the folded pulsar archives and derived ToAs with PSRCHIVE¹³ (Hotan et al. 2004), including the polarisation calibration of Parkes observations with pac. We performed our timing model fits with TEMPO2¹⁴ (Hobbs et al. 2006).

To break the degeneracy between DM and spin evolution, we implemented a frequency-resolved timing strategy. MeerKAT L-band and UHF observations were reduced into two frequency sub-bands of equal width, while Murriyang UWL observations were divided into three sub-bands: low (723–1093 MHz), mid (1094–1825 MHz), and high (1826–2656 MHz). Due to faintness at high frequencies, MeerKAT S-band ToAs were integrated over the full band. This scheme also isolated scattering effects in the lowest-frequency band.

Timing templates were derived with PSRCHIVE’s paas from the full time addition of all Murriyang observations included in this study. Templates were generated for the individual low-, mid-, and high-frequency Murriyang UWL timing sub-bands stated above, and also for the stated MeerKAT L-band, S-band, and UHF timing sub-bands from the overlapping Murriyang UWL sub-bands. In this way, all timing templates were derived from a single, coherent data set.

In the timing models, we accounted for the spin frequency, ν , and its first two time derivatives, $\dot{\nu}$ and $\ddot{\nu}$, the DM and its first derivative, DM_0 and DM_1 , and a global timing jump between MeerKAT and Murriyang. For the binaries, we used the ELL1 timing model (Lange et al. 2001), which implements the eccentricity parameters $\eta = e \sin \omega$ and $\kappa = e \cos \omega$ (where e and ω are the Keplerian eccentricity and angle of periastron parameters), as well as the time of the ascending node, T_A , the projected semi-major axis, x , and the orbital period P_b . We also included the orbital period derivative, \dot{P}_b , sky position RA and DEC (J2000), and the proper motion parameters, μ_{RA} and μ_{DEC} .

The timing residuals are shown in Figure 3. Tables D.1 and D.2 present the complete fit and derived parameters. In the cases of pulsars A, E, and H, we removed some MeerKAT ToAs to mitigate significant time-variable scattering effects, which resulted in inconsistencies between the MeerKAT and Murriyang ToAs. For A and E, which are bright pulsars with high-quality Murriyang UWL timing, we excluded the MeerKAT ToAs from the analysis, incurring only a marginal loss in precision. For H, removing MeerKAT ToAs below $f < 1.0$ GHz while retaining

⁹ <https://github.com/BezuidenhoutMC/SeeKAT>

¹⁰ https://github.com/mcbernadich/pulsar_orbit_solver

¹¹ <https://github.com/pfreire163/Dracula>

¹² <https://github.com/demorest/dspsr>

¹³ <https://psrchive.sourceforge.net/>

¹⁴ <https://www.pulsarastronomy.net/pulsar/software/tempo2>

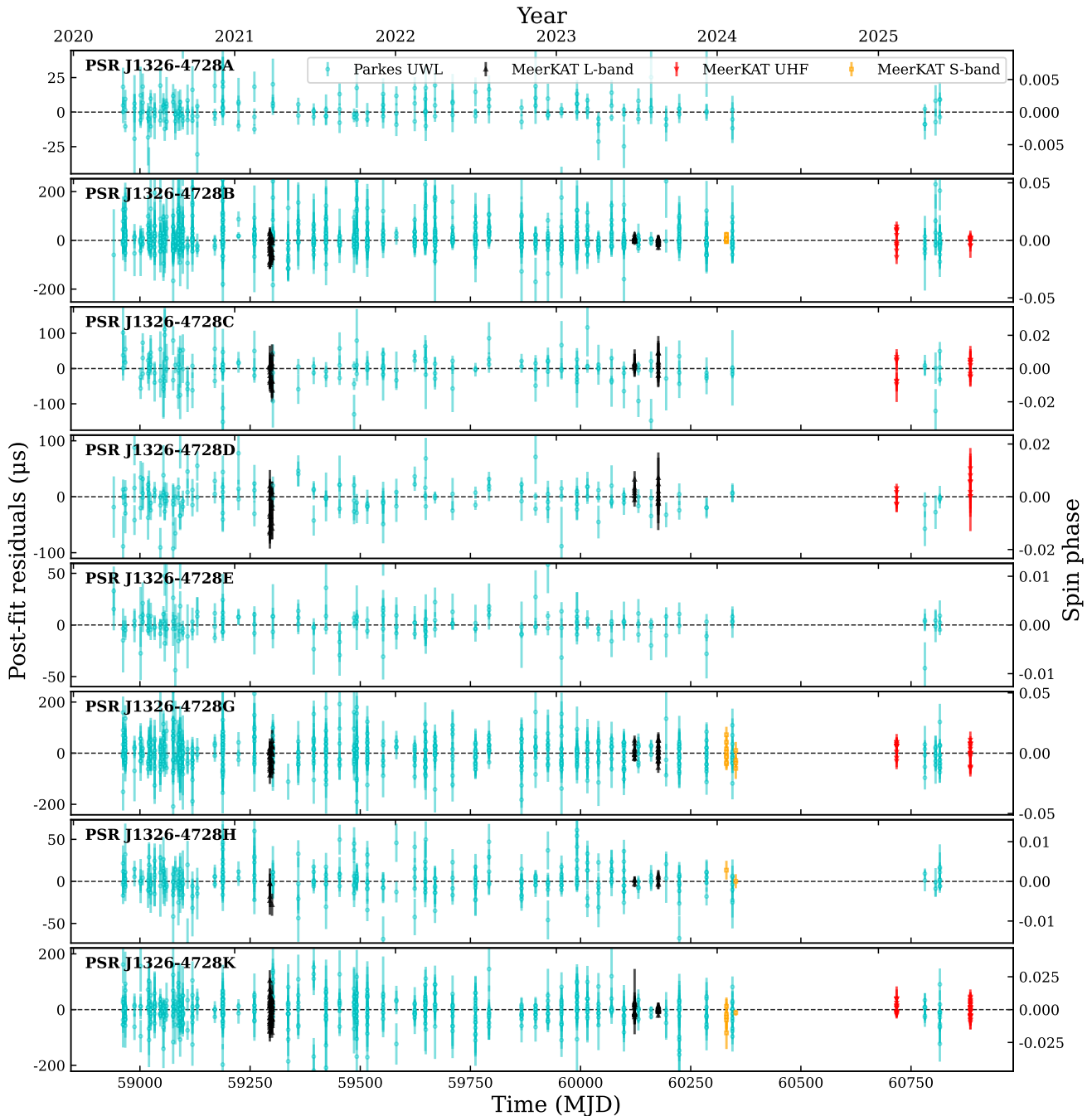


Fig. 3: Combined MeerKAT and Murriyang timing residuals for A, B, C, D, E, G, H, and K as a function of time. A global timing jump between the two telescopes has been applied.

higher-frequency L-band and S-band ToAs was sufficient to obtain a consistent timing solution. We could not derive significant S-band ToAs for C and D. Finally, we applied uncertainty multipliers ($\sigma'_{\text{ToA}} = \text{EFAC} \times \sigma_{\text{ToA}}$) to the MeerKAT and Murriyang ToAs to ensure reduced χ^2 values close to unity.

4.2. Orbital solutions

For I, despite frequent detections with Murriyang, we were unable to derive a phase-coherent timing solution. For the remaining pulsars, Murriyang observations did not yield sufficiently frequent high signal-to-noise detections, and the large gaps between MeerKAT observations prevented the achievement

of phase connection. Nevertheless, the MeerKAT ToAs allowed us to obtain precise orbital parameters for I, L, N, and Q.

The solutions were fit to frequency-integrated MeerKAT ToAs with TEMPO2. At each observation, we allowed the fitting of an arbitrary time offset (timing jumps) to allow global fitting despite the lack of phase-connection. Timing templates were derived with PSRCHIVE's paas from high signal-to-noise detections in individual observations. We modelled N with the Keplerian parameters of the Damour-Deurelle binary model (DD, Damour & Deruelle 1986), implementing e , ω , and the time of passage of periastron, T_0 . For I, L, and Q, we used the ELL1 timing model. For Q, the S-band observations, and the 28 July 2025 UHF observation are excluded due to non-detections de-

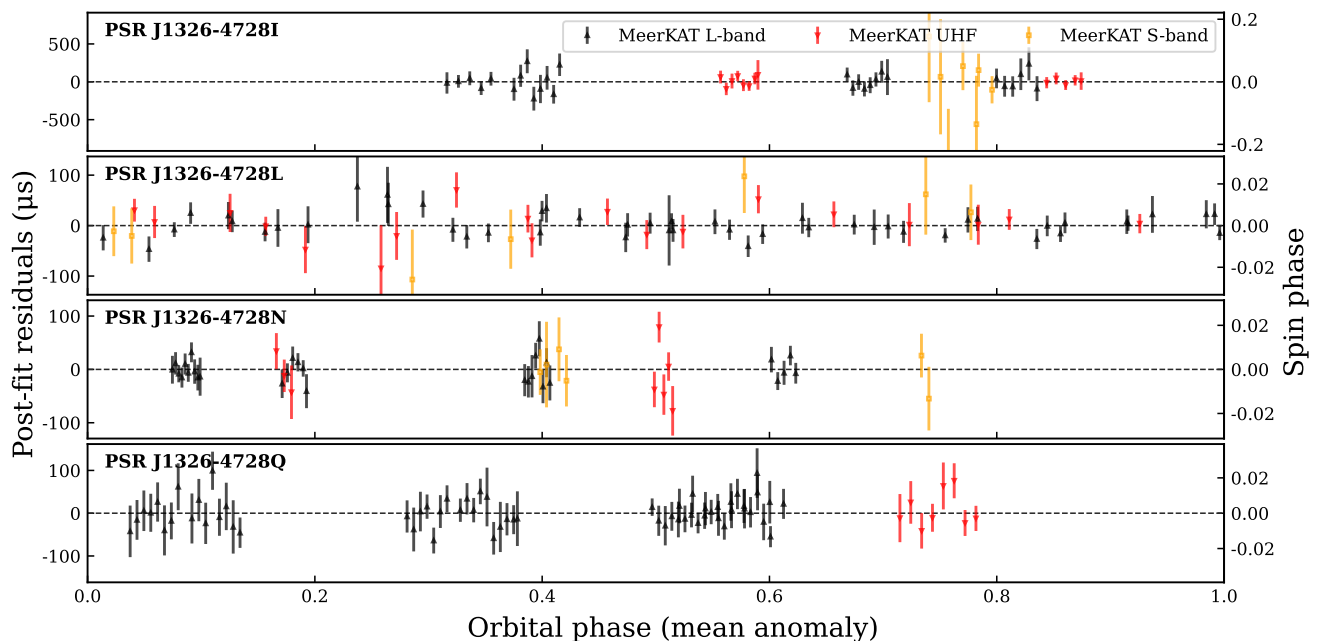


Fig. 4: MeerkAT timing residuals for I, L, N, and Q, plotted as a function of orbital phase (0–1). Included observations comprise all TRAPUM MeerkAT epochs, except for the S-band and 28 July 2025 UHF observations for Q, and including the additional PTUSE 14 February 2024 observation for L. Timing jumps have been applied between observations.

spite blind PRESTO periodicity searches. For L, its dedicated 14 February 2024 PTUSE MeeTIME L-band observation was also included to improve the orbital description.

Figure 4 shows the timing residuals against orbital phase, with per-epoch timing jumps implemented. The complete fit and derived parameters are shown in Table D.3. Pulsars I, N, and Q have long orbital periods, with orbital coverage fairly evenly distributed. L, with a shorter orbit, has full orbital phase coverage.

5. Searches for high-energy emission counterparts

5.1. Fermi LAT analysis of γ -rays

ω Cen is associated with *Fermi* Large Area Telescope (LAT, Atwood et al. 2009) source 4FGL J1326.6–4729. Similar to the analysis of A–E in Dai et al. (2023), we folded the γ -ray photons of A, G, H, and K. Relative to the LAT PSF, the MSP position offsets from the point source are negligible. We used 17 yr of P8_R3_SOURCE 8 data (Atwood et al. 2013; Bruel et al. 2018), selecting events with reconstructed direction within 3 deg of the cluster centre and reconstructed energies in the range 100 MeV to 30 GeV. We used the 4FGL-DR4 sky model (Abdollahi et al. 2022; Ballet et al. 2023) to estimate photon weights (Bickel et al. 2008), and the probability that a photon is associated with γ -ray source or background sources. Using the timing solutions, we computed the photon phase (Ray et al. 2011) and calculated the weighted H-test statistic (Kerr 2011). We found for all 4 pulsars $H < 7$, indicating no detections.

We determine the maximum amount of the γ -ray flux from 4FGL J1326.6–4729 that any individual pulsar could have via Monte Carlo simulations. For each pulsar in A–E, G, H, and K, we assume a typical pulse profile (Smith et al. 2023), $f(\phi)$, composed of two Gaussians with widths σ separated by 0.45 in phase and with a flux ratio of 1.5, and a pulsed and un-pulsed components with contributions w and $1 - w$. For each experiment, we draw a uniform random variable $u \in [0, 1]$ and assign the photon to the background if $u > w$, otherwise to the source. For the

photons assigned to the pulsar, we draw a phase randomly from $f(\phi)$, and we then calculate H . We increase w from 0 to 0.2, at a 0.01 step, considering that a pulsar would be detectable when the median H-test exceeds 25. We find a typical w threshold of 10–12% for values of σ of 0.02–0.03. That is, unless the pulse profile is unusually broad, no more than about 10% of the total γ -ray flux comes from any of the searched individual pulsars.

5.2. X-rays

Dai et al. (2023) reported that the timing sky positions of pulsars A, B, C, and E coincide with *Chandra* sources (Henleywillis et al. 2018; Zhao & Heinke 2022). Using our updated timing positions (Table D.2) we further find that G and K are 1σ consistent with the *Chandra* sources 24f and 21d (with positional uncertainties of $\sim 0.4''$) in Henleywillis et al. (2018). G is also coincident with ATCA radio source 4, whose position is reported in Dai et al. (2023). H shows a marginal $\sim 3\sigma$ positional consistency with source 14c. Finally, L, based on its localised position reported in Chen et al. (2023), could potentially be associated with source 32d at the $\sim 3\sigma$ level. The pulsar timing positions are compared with their respective counterparts in Figures E.1 and E.2 (Appendix E). Motivated by these positional overlaps, we performed X-ray pulsation searches and flux limits.

5.2.1. NICER analysis

ω Cen was observed 23 times in 2023–2025 with *NICER*¹⁵ (Gendreau et al. 2012). The main target of these observations was the quiescent LMXB found by Rutledge et al. (2002), located on the East side of the cluster. The *NICER* field of view (FoV) is 30 arcmin² and contains A, G, H, and K (Figure E.1).

¹⁵ <https://science.nasa.gov/mission/nicer/>

We downloaded all observations and applied the `nicer12` pipeline¹⁶. The observations were all done after the onset of the light leak issue¹⁷, and some of them had nominal 0 exposure due to the conservative default conditions of the pipeline on the acceptable undershoot rates. In principle, the light leak should not heavily affect pulsar searches, and therefore, we tried to use more permissive conditions in order to recover part of the exposure time by tweaking the `threshfilter`, `underonlyscr`, `mpugtiscr`, `lowmemscr` options. However, we could not improve the available exposure by more than 10%.

We used the best available radio solutions (from this work or Dai et al. 2023) as references, including a TZRMJD value corresponding to a reference radio ToA. We folded all NICER data with PINT's (Luo et al. 2021) `photonphase` script. For each observation, we gave as input the NICER event list, the orbit file, and the parameter files for the radio solution. We used the `-addphase` option to save the pulse phase of each photon to an output file, and we calculated total histograms of pulse phases from all 23 observations. We calculated the H test (de Jager et al. 1989) to search for any modulation of the X-ray flux, but found no evidence for a pulsed signal.

5.2.2. XMM-Newton analysis

XMM-Newton¹⁸ observed ω Cen for 40 ks in 2001 to investigate the faint X-ray sources in the GC (Gendre et al. 2003). We aimed to constrain the X-ray emission from radio positions.

We reduced the observation using `pysas-1.4.8`, a Python wrapper of XMM Scientific Analysis System (XMMSSAS). We reprocessed the data using the current calibration files and extracted images from the PN, MOS1, and MOS2 detectors. To quantify the X-ray emission, we demarcated circles of 4'' around individual pulsar positions and extracted the photon events from these regions. In all cases except one, we find that the observed integrated counts are consistent with the typical background level in the cluster of 56 ± 7 , sampled from random points with no excess. For N, we observe a contamination from a nearby X-ray source (J132648.725–473124.90), also identified in deep Chandra observations (source 331 in Henleywillis et al. 2018, also shown in Figure E.1).

The background count rate is $\sim 5.5 \times 10^{-4}$ counts s^{-1} , which corresponds to a net absorbed flux of 5.3×10^{-15} ergs $cm^{-2} s^{-1}$. This upper limit is consistent with the estimated fluxes from the Chandra observation (Henleywillis et al. 2018), which have recorded fainter objects of $\sim 10^{-16}$ ergs $cm^{-2} s^{-1}$ in their survey. We conducted a source detection search and cross-matched the detections with the radio pulsar positions, but we found no counterparts at the pulsar positions.

6. Discussion

6.1. Dynamical constraints on ω Cen

6.1.1. The acceleration field of ω Cen

As is commonly done in GCs (e.g. Prager et al. 2017; Freire et al. 2017; Dai et al. 2023), we constrain the acceleration field in ω Cen from the measured $\dot{\nu}$ values. To convert the spin-period derivatives, $\dot{P}_s = -\dot{\nu}/\nu^2$, into constraints on the cluster LOS acceleration $a_{LOS,c}$, we first compute Shklovskii effect

¹⁶ https://heasarc.gsfc.nasa.gov/docs/nicer/analysis_threads/nicer12/

¹⁷ https://heasarc.gsfc.nasa.gov/docs/nicer/analysis_threads/light-leak-overview/

¹⁸ <https://www.cosmos.esa.int/web/xmm-newton>

and Galactic acceleration field contributions (Shklovskii 1970; Damour & Taylor 1991)

$$\frac{\dot{P}_{Sh}}{P_s} = \frac{1}{c} |\boldsymbol{\mu}|^2 d, \quad \frac{\dot{P}_G}{P_s} = \frac{1}{c} \mathbf{K}_0 \cdot (\mathbf{a}_{\omega Cen} - \mathbf{a}_{SSB}), \quad (1)$$

where c is the speed of light, $\boldsymbol{\mu}$ is the proper-motion vector, \mathbf{K}_0 is the unit vector from the solar-system barycentre (SSB) to ω Cen, and $\mathbf{a}_{\omega Cen}$ and \mathbf{a}_{SSB} are the Galactic accelerations at the locations of the cluster and the SSB, respectively.

We adopt the values measured proper motions (Tables D.1 and D.2) and the dynamical cluster distance of $d = 5494 \pm 61$ pc (Häberle et al. 2025). The resulting Shklovskii contributions span $(1.2\text{--}5.5) \times 10^{-10}$ $m s^{-2}$ across the pulsar sample. The Galactic acceleration contribution is computed using the Galactic potential of McMillan (2017), assuming a Galactocentric distance of 8.2 kpc for the SSB and the cluster distance quoted above. This yields a relative LOS acceleration of -1.04×10^{-10} $m s^{-2}$. Given the absence of significant $\dot{\nu}$ measurements indicative of local perturbations, and the relatively low stellar density of ω Cen, we neglect acceleration contributions from nearby objects.

The dominant source of uncertainty in the above contributions arises from the measured proper motions, which exceed the uncertainty from the dynamical distance by two orders of magnitude and that from the Galactic potential model by roughly one order of magnitude. We therefore propagate only the proper-motion uncertainties into each pulsar's LOS acceleration term.

After applying these corrections, upper limits on the cluster-induced LOS acceleration are obtained as

$$a_{LOS,c} < c \times (\dot{P}_s - \dot{P}_{Sh} - \dot{P}_G), \quad (2)$$

where the upper-limit nature arises because the intrinsic pulsar spin-down, which is degenerate with the cluster acceleration and cannot be independently quantified.

We use the constrained accelerations to test the compatibility of the pulsars with a King model density and potential (King 1962). Following Freire et al. (2005) and Dai et al. (2023), we adopt a King model for the mass distribution, which yields a radial acceleration field

$$a_c(r') = \frac{9\sigma_v^2 d}{r_c} \frac{1}{r'^2} \left(\frac{r'}{\sqrt{1-r'^2}} - \sinh^{-1} r' \right), \quad (3)$$

where σ_v is the central velocity dispersion, r_c is the core radius, $r' = r/r_c$ is the distance from the cluster centre normalised by the core radius, and d is the cluster distance, which we take to be $d = 5494$ pc from the dynamical measurement of Häberle et al. (2025). From this, and assuming $r_c = 2.88'$ (Baumgardt & Hilker 2018) and $\sigma_v = 0.81$ $mas yr^{-1}$ (Häberle et al. 2025), we derive the maximum and minimum expected values of $a_{LOS,c}$ as a function of projected angular separation from the cluster centre, θ .

The resulting upper limits on $a_{LOS,c}$ are reported in Tables D.1 and D.2, and are shown in Figure 5 as a function of projected angular separation from the cluster centre. The figure also displays the maximum and minimum LOS accelerations expected from the King model. For completeness, we have also added the limits imposed by the King model assuming $\sigma_v = 0.70$ $mas yr^{-1}$ (Baumgardt & Hilker 2018), as it was done Dai et al. 2023, as well as the maximum and minimum contributions from central compact objects of different masses.

We find that pulsars in ω Cen with measured \dot{P}_s are consistent with the updated King-model cluster mass distribution. H, B, and D are the only potential outliers, with upper limits that may place the pulsars outside of the potential if $\sigma_v = 0.7$ $mas yr^{-1}$, but that are well contained if $\sigma_v = 0.81$ $mas yr^{-1}$.

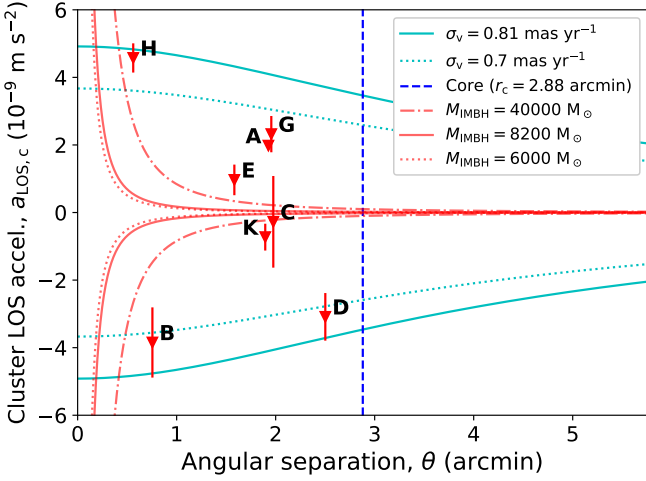


Fig. 5: Upper limits on LOS accelerations for pulsars against angular separation from the cluster centre. The plot also shows the maximum and minimum LOS accelerations expected from the King potential, assuming σ_v and r_c from Baumgardt & Hilker (2018) and Häberle et al. (2025), as well as the contributions from central compact masses of 6000, 8200, and $4 \times 10^4 M_{\odot}$.

6.1.2. Constraints on the central IMBH

Häberle et al. (2024) present evidence for a central compact object of at least $8200 M_{\odot}$ based on stellar proper motions within the central parsec. In contrast, Bañares-Hernández et al. (2025) favour an extended central mass and place an upper IMBH limit of $6000 M_{\odot}$ from multiple astrometric measurements, including the timing measurements from Dai et al. (2023).

The pulsars analysed in our work lie outside the region of influence of an IMBH with mass 10^3 – $10^4 M_{\odot}$. Figure 5 illustrates the maximum and minimum LOS acceleration contributions expected from central point masses of 8200 and $6000 M_{\odot}$. Even for pulsars H and B, the closest to the cluster centre, at angular separations of $\theta = 0.56'$ and $0.76'$, the acceleration induced by an IMBH in this mass range would be marginal compared to the broader cluster contribution. H and B would, however, be sensitive to an IMBH larger than $10^4 M_{\odot}$, as exemplified in Figure 5 by the maximum contribution from a central mass of $4 \times 10^4 M_{\odot}$.

To quantify this, we perform a likelihood analysis for black hole masses from 0 to $10^6 M_{\odot}$,

$$\mathcal{L}(M_{\text{BH}}) = \prod_{\text{PSR}} p(a_{\text{LOS},c}, \theta | M_{\text{BH}}), \quad (4)$$

where $p(a_{\text{LOS},c}, \theta | M_{\text{BH}})$ is the probability of a pulsar exhibiting a LOS acceleration $a_{\text{LOS},c}$ at angular separation θ , assuming the King density profile,

$$\rho(r') = \frac{\rho_0}{(1 + r'^2)^{3/2}}, \quad (5)$$

where ρ_0 is the central density, and the cluster gravitational field from equation 3 ($\sigma_v = 0.81 \text{ mas yr}^{-1}$, $r_c = 2.88'$) with the addition of a contribution from a central mass M_{BH} ,

$$a_{\text{BH}}(r) = G \frac{M_{\text{BH}}}{r^2}. \quad (6)$$

We compute probability distributions for the true values of $a_{\text{LOS},c}$ given our measured upper limits. The surface magnetic

field strengths (B_s) of GC MSPs follow a log-normal distribution with $\mu_{\log B} = 8.47$ and $\sigma_{\log B} = 0.33$ (Prager et al. 2017). Assuming a braking index $n = 3$, we convert this into a distribution for the intrinsic spin-down ($\dot{P}_{s,\text{int}}$) contribution to the observed LOS acceleration,

$$a_{\text{int}} = c \left(\frac{\dot{P}_{s,\text{int}}}{P_s} \right) = 7.96 \times 10^{-10} \left(\frac{B_s}{2 \times 10^8 \text{ G}} \right)^2 \left(\frac{2 \text{ ms}}{P_s} \right)^2 \text{ m s}^{-2}, \quad (7)$$

which is incorporated into $p(a_{\text{LOS},c}, \theta | M_{\text{BH}})$. In addition, we also account for the Gaussian uncertainties given by the 1σ uncertainties in the Shklovskii term (see the previous section).

The resulting likelihood peaks at $M_{\text{BH}} = 0 M_{\odot}$ and declines until $4 \times 10^4 M_{\odot}$, after which it drops sharply. This confirms that the observed \dot{P}_s values are not sensitive to an IMBH in the 10^3 – $10^4 M_{\odot}$ range. Nevertheless, we place an upper limit of $M_{\text{BH}} < 10^5 M_{\odot}$ at 90% confidence.

6.1.3. Proper motions and higher spin derivatives

The measured pulsar proper motions (Tables D.1 and D.2) are broadly consistent with the known kinematics of the cluster. Their mean values and standard deviations are $\langle \mu_{\text{RA}}, \mu_{\text{DEC}} \rangle = -4.2 \pm 1.2, -8.5 \pm 2.7 \text{ mas yr}^{-1}$, which coincides with the bulk motion of Omega Centauri, $\mu_{\text{RA}}, \mu_{\text{DEC}} = -3.1925, -6.7445 \text{ mas yr}^{-1}$ (Gaia Collaboration et al. 2018).

Some pulsars also show a tentative second spin-frequency derivative measurements in the range $\ddot{\nu} \sim 10^{-26}$ – $10^{-25} \text{ Hz s}^{-1}$, larger than predicted by second-order Shklovskii or Galactic gravitational field effects. However, they have low significance and may be spurious. We therefore refrain from interpreting these values until more precise constraints become available.

6.2. The pulsar population of ω Cen

6.2.1. The encounter rates of ω Cen

The total stellar encounter rate in a GC, Γ , is expected to be a predictor of its overall MSP content (Hui et al. 2010; Bahramian et al. 2013). If pulsar recycling is driven by the formation of close binaries in encounters, the MSP population should scale as $\Gamma \propto \rho_c^{3/2} r_c^2$, where ρ_c is the core density (Verbunt & Hut 1987). For ω Cen, we adopt $\rho_c = 1.7 \times 10^{-3} M_{\odot} \text{ pc}^{-3}$ and $r_c = 4.30 \text{ pc}$ (Baumgardt & Hilker 2018). Normalising to M4 (NGC 6121, $\rho_c = 9.8 \times 10^{-3} M_{\odot} \text{ pc}^{-3}$, $r_c = 0.45 \text{ pc}$, $\Gamma_{\text{M4}} \equiv 1$), we obtain a moderate $\Gamma_{\omega \text{ Cen}} = 6.6$.

By contrast, the encounter rate per individual binary, γ , quantifies the likelihood that an existing binary will undergo further interactions, producing eccentric systems, exchanges, or complete disruption. This is expected to scale as $\gamma \propto \rho_c^{1/2} r_c^{-1}$ (Verbunt & Freire 2014). Normalising to M4 yields a very low value of $\gamma_{\omega \text{ Cen}} = 0.044$, reflecting the low density of ω Cen.

6.2.2. The binary population

We now have measured the orbital properties of all eight known binary MSPs in ω Cen. Figure 6 compares their orbital and spin parameters (from Table 1) with those of Galactic field binaries from the ATNF pulsar catalogue¹⁹ (Manchester et al. 2005). Pulsars B, G, H, K, and L exhibit several defining properties of black widow systems (see Roberts 2013; Blanchard et al. 2025): they are fully recycled ($P_s < 5 \text{ ms}$), have very short orbital periods

¹⁹ <http://www.atnf.csiro.au/research/pulsar/psrcat>

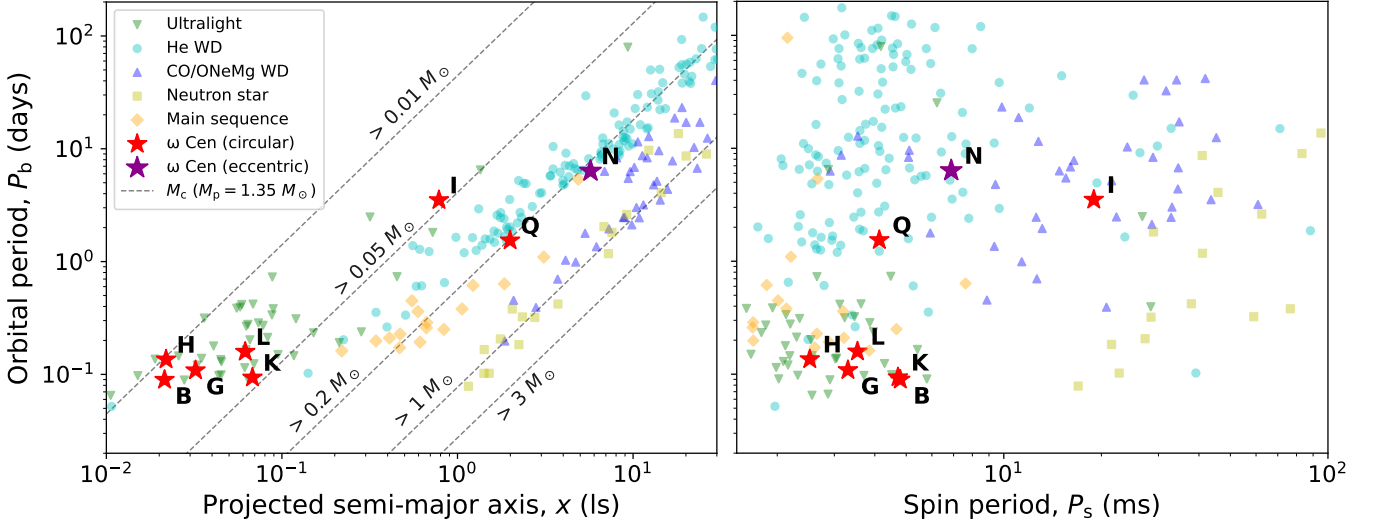


Fig. 6: Orbital and spin properties of binary pulsars in ω Cen compared with the Galactic binary populations. The Galactic pulsar parameters and companion nature are taken as listed by the ATNF (Manchester et al. 2005, retrieved in March 2024). **Left:** orbital period versus projected semi-major axis, with lines of equal minimum companion mass drawn. **Right:** orbital versus spin period.

($P_b < 1$ day), extremely circular orbits ($e \lesssim 10^{-4}$), and very low-mass companions ($M_c < 0.1 M_\odot$).

Several of these systems also display eclipsing behaviour characteristic of black widows (e.g. Fruchter et al. 1988; Abbate et al. 2024). G, K, and L show recurring eclipses at superior conjunction, while B exhibits eclipses across a wide range of orbital phases. A dedicated study of eclipses in ω Cen is currently in preparation (Colom i Bernadich et al., in prep.)

Additionally, K shows significant orbital period evolution of $\dot{P}_b = 6.25(\pm 0.19) \times 10^{-12} \text{ s s}^{-1}$ (Table D.2), a behaviour commonly observed in black widow systems (e.g. Shaifullah et al. 2016). This measurement is not spurious, as the exclusion of \dot{P}_b from the model leads to noticeable Rømer delay residual amplitudes across orbital phase in the MeerKAT ToAs. The measured value exceeds expectations from general relativistic effects, the Shklovskii contribution, or the cluster gravitational potential, indicating instead that it is driven by interactions with material expelled from the companion.

The apparent overabundance of black widow systems in ω Cen is noteworthy. King et al. (2003) proposed that this excess in GCs arises from secondary stellar encounters, in which the original low-mass companion that recycled the MSP is replaced by a more massive turn-off star. Subsequent stellar encounters may harden the resulting binary even further, and Roche-lobe overflow and envelope expulsion through stellar winds then shrink and circularise the orbit via tidal interactions. Alternatively, close encounters may have instead hardened neutron star - main sequence progenitor binaries (Heggie 1975; Hills 1975).

However, these formation channels are uncertain in ω Cen. The timescale for a binary to experience a stellar encounter with impact parameter r can be estimated as (King et al. 2003)

$$\tau \approx 7 \times 10^{10} \text{ yr} \left(\frac{10^5 \text{ pc}^{-3}}{n} \right) \left(\frac{\sigma_v}{10 \text{ km s}^{-1}} \right) \left(\frac{R_\odot}{r} \right) \left(\frac{M_\odot}{m} \right), \quad (8)$$

where $n = 3.7 \times 10^3 \text{ pc}^{-3}$ is the stellar density, estimated from the core mass density of $1.7 \times 10^3 M_\odot \text{ pc}^{-3}$ (Baumgardt & Hilker 2018) and a mean stellar mass of $M_* = 0.45 M_\odot$ derived from the stellar mass function of ω Cen (Sollima et al. 2007), and $m = M_p + M_c + M_*$ is the combined binary and interloper mass.

Assuming a typical pulsar binary with $P_b = 1\text{--}10$ days, a companion mass of $M_c = 0.25 M_\odot$, and an encounter distance comparable to the orbital separation, we obtain encounter timescales of $\tau = 10^2\text{--}10^3$ Gyr, far exceeding the cluster’s age. Furthermore, likely multiple encounters are needed to process a binary into a black widow.

Unless ω Cen has a budget of several thousands of neutron stars in binaries that could potentially be turned into black widows (a requirement difficult to reconcile with estimates of neutron star retention and binary fractions) it is unlikely that the five observed black widows formed in the currently observed environment. Reducing τ below the Hubble time ($\tau \lesssim 10$ Gyr) would require densities of $10^4\text{--}10^5 M_\odot \text{ pc}^{-3}$. As an alternative, several studies have shown that black widows can form through the evolution of low-mass X-ray binaries or other compact systems without stellar encounters (Chen et al. 2013; Benvenuto et al. 2015; Guo et al. 2022). Nevertheless, ω Cen still has an overabundance of black widows compared to the Galactic field, where binaries also evolve largely without interactions, posing an interesting conundrum.

Pulsars I and Q, on the other hand, are wider circular binaries. As shown in Figure 6, Q is a textbook example of an MSP with $P_s < 5$ ms and $P_b > 1$ day in a circular orbit, hosting a $M_c > 0.2 M_\odot$ He white dwarf companion, likely formed through a low-mass X-ray binary phase (see Tauris & Savonije 1999). Pulsar I is more unusual, with a longer spin period of $P_s \sim 20$ ms and a $M_c < 0.1 M_\odot$ companion, but it nevertheless resides in a circular orbit with $P_b \sim 3.5$ days. These properties are consistent with binary evolution unaffected by stellar encounters.

Pulsar N has the widest orbit and a pronounced eccentricity of $e = 0.093$. With a low companion mass of $M_c \sim 0.25 M_\odot$ and a spin period of $P_s = 6.88$ ms, the companion is likely a He white dwarf, implying that the eccentricity did not originate from a second supernova event. Owing to the large positional uncertainty of N from the lack of a timing solution, we are unable to determine whether the companion could instead be a main-sequence star, although this scenario is disfavoured.

Assuming N was originally a circular binary, we examine whether its eccentricity can be reconciled with the encounter

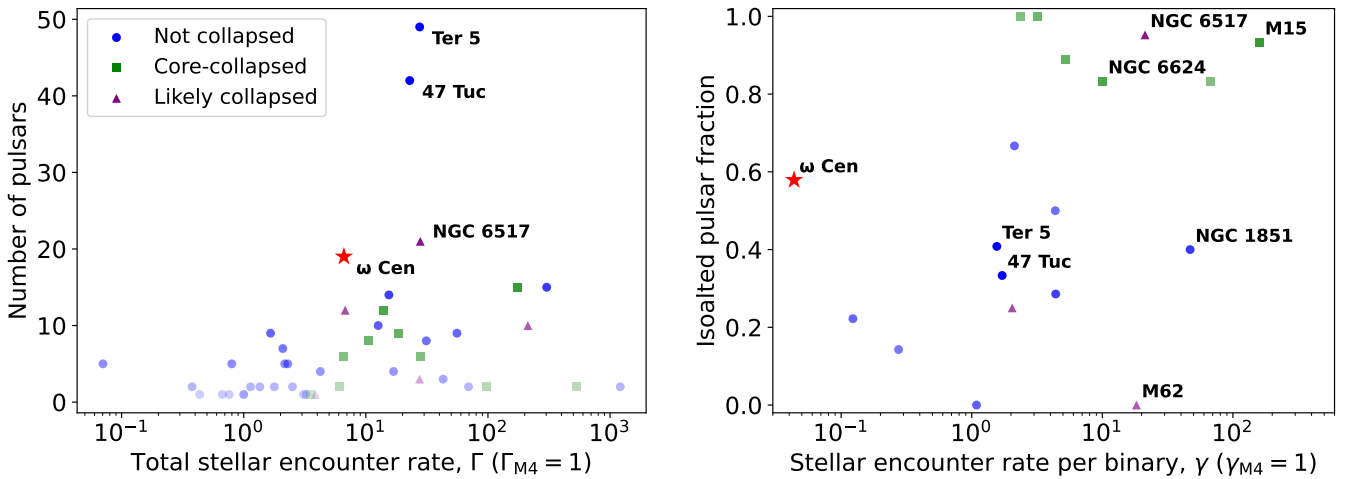


Fig. 7: Pulsar populations in globular clusters as a function of stellar encounter rate. Left: total number of pulsars versus the global encounter rate, with well-studied clusters highlighted. Right: fraction of isolated pulsars versus the encounter rate per binary for clusters hosting at least five pulsars. Pulsar data are taken from <https://www3.mpifr-bonn.mpg.de/staff/pfreire/GCpsr.html>, cluster parameters from Baumgardt & Hilker (2018), and core-collapse classifications from Harris (2010). NGC 6517 is treated as core-collapsed in several studies (e.g. Verbunt & Freire 2014; Yin et al. 2024), despite not being classified as such by Harris (2010).

rate in ω Cen. Rasio & Heggie (1995) predict that the eccentricities of MSP binaries in GCs grow over time due to stellar fly-bys, with higher stellar densities per binary and longer orbital periods producing larger eccentricities. Adopting again $n = 3.7 \times 10^3 \text{ pc}^{-3}$ and $\sigma_v = 21.1 \text{ km s}^{-1}$, and inserting these values into (Rasio & Heggie 1995)

$$e \approx \text{Max} \left\{ \left(\frac{\eta}{400} \right)^{5/2} \left(\frac{P_b}{\text{day}} \right)^{5/3}, 4 \exp \left[- \left(\frac{\eta}{200} \right)^{-3/2} \left(\frac{P_b}{\text{day}} \right)^{-1} \right] \right\}, \quad (9)$$

where

$$\eta = \left(\frac{t_{\text{age}}}{10^9 \text{ yr}} \right) \left(\frac{n}{10^4 \text{ pc}^{-3}} \right) \left(\frac{10 \text{ km s}^{-1}}{\sigma_v} \right), \quad (10)$$

and assuming an age of ~ 9 Gyr, we find a maximum eccentricity induced by stellar encounters of $e < 10^{-5}$, much smaller than the observed value. Again, reproducing the eccentricity of N would require a density of at least several $10^{-4} \text{ M}_{\odot} \text{ pc}^{-3}$.

Alternatively, the eccentricity of N may be explained by a third body in a hierarchical triple system, as proposed for a small population of eccentric Galactic MSPs with low-mass He white dwarf companions (see Grunthal et al. 2024). If the tertiary remains bound on a wide orbit, its presence could be revealed by high-order spin-frequency derivatives in future timing analyses (e.g. Dutta et al. 2025).

6.2.3. General pulsar populations

With 19 confirmed MSPs (including S), ω Cen hosts a millisecond-pulsar population broadly consistent with the total number expectation. The left plot of Fig. 7 compares its total MSP content and $\Gamma_{\omega \text{ Cen}}$ with those of other well-studied GCs, such as NGC 6517, 47 Tuc, and Ter 5 (e.g. Yin et al. 2024; Freire et al. 2017; Padmanabh et al. 2024), as a function of their respective Γ values, computed using structural parameters from the Baumgardt & Hilker (2018) catalogue²⁰. The currently known MSP population ω Cen is consistent with its Γ parameter.

²⁰ <https://people.smp.uq.edu.au/HolgerBaumgardt/globular/>

The total MSP population of ω Cen is also consistent with its measured γ -ray luminosity. From the $L_{\gamma} = 3.6 \times 10^{34} \text{ erg s}^{-1}$ γ -ray emission of ω Cen, and assuming an average MSP spin-down power of $1.8 \times 10^{34} \text{ erg s}^{-1}$ and a γ -ray efficiency of 0.08, de Menezes et al. (2019) predicted an MSP population of ~ 25 for ω Cen, remarkably close to the currently known population. Notably, this prediction was made prior to the first pulsar discoveries in the cluster (Dai et al. 2020).

The large fraction of isolated MSPs is, however, surprising, as first highlighted by Chen et al. (2023). 11 of the 19 confirmed MSPs in ω Cen are isolated, in apparent contradiction with its very low stellar encounter rate per individual binary. The discrepancy becomes even more striking when ω Cen is compared with other GCs. The right-hand panel of Figure 7 shows the fraction of isolated MSPs in clusters hosting at least ten pulsars as a function of their γ values. In general, core-collapsed GCs or GCs with extreme γ values, such as NGC 6624, NGC 6517, and M15, are almost entirely dominated by isolated pulsars (Yin et al. 2024; Abbate et al. 2022; Wu et al. 2024), while non-collapsed clusters with moderate γ values result in a more balanced composition. In contrast, ω Cen stands out as a clear outlier: despite having the lowest γ among all plotted clusters by more than an order of magnitude, it exhibits an isolated MSP fraction of ~ 0.58 , exceeding that of 47 Tuc, Ter 5, or NGC 1851, whose γ are several orders of magnitude higher.

6.2.4. A hint of a hidden history in ω Cen

The over-abundance of black widow systems, the large eccentricity of N, and the large fraction of isolated MSPs in a low-density cluster such as ω Cen remain difficult to reconcile.

This puzzle does not go away even if we account for the biases in our searches. Our search strategies (here and in Chen et al. 2023) favour the detection of isolated pulsars and wide binaries ($P_b > 1 \text{ day}$) over compact binary systems. The latter are only detectable as highly accelerated or jerked signals in short observational segments, whereas isolated or mildly accelerated pulsars can accumulate their signals over several hours. However, assuming a flux distribution of $\propto S^{-2}$ for GC MSPs

(McConnell et al. 2004), this results only in the loss of $\sim 40\%$ of binary systems with $P_b = 4$ hours. Even assuming 3–5 undetected compact binaries, the 11 isolated pulsars still constitute a large fraction. Furthermore, the same bias applies to the MSP populations of other GCs, so this is unlikely to affect comparisons across clusters.

There has been discussion on the possibility of isolated MSPs arising from the evolution of black widow systems. One speculative formation channel is the complete ablation of the companion in black widow binaries (van den Heuvel & van Paradijs 1988), although this scenario remains poorly constrained. A recently proposed alternative explains the isolated MSP population of ω Cen via the efficient disruption of black widow systems during stellar encounters, owing to the low mass of their companions (de Menezes 2026). However, while these channels offer plausible explanations for the formation of isolated MSPs, they implicitly rely on an even larger parent population of black widows. As discussed in Section 6.2.2, the present-day stellar density of ω Cen appears insufficient to sustain such an elevated black widow formation rate.

These discrepancies indicate that present-day encounter parameters alone are not reliable predictors of the composition of GC MSP populations, and that additional factors likely play an important role. A clear example, opposite to ω Cen, is M62, a GC with a γ value comparable to that of core-collapsed clusters, yet whose known MSP population is entirely composed by binaries (Figure 7, Vleschower et al. 2024).

In this context, it is plausible that a fraction of the MSPs in ω Cen formed in a denser environment than that observed today. ω Cen exhibits the greatest stellar population diversity among Galactic GCs and is widely considered to be the remnant nucleus of a former dwarf galaxy. Such diversity may reflect past episodes of star formation, mergers, or dynamical evolution associated with its progenitor system (Calamida et al. 2020). Furthermore, nuclear clusters in low-mass galaxies are thought to form, at least in part, through the in-spiral of globular clusters toward galactic centres (Neumayer et al. 2020; Fahrion et al. 2021), providing an additional pathway to the structural and dynamical complexity observed in ω Cen.

7. Conclusions

In this work, we present an updated view of the pulsar population of ω Cen. New pulsar searches of the ATCA-dedicated beams from the 21 March 2021 MeerKAT L-band observation and the tiling beams from the 11 February 2025 MeerKAT UHF observation resulted in the discovery of pulsar S, a new isolated millisecond pulsar.

We provide updated orbital parameters for all known binaries in the cluster, revised timing solutions for A–E, and new solutions for G, H, and K, all with significant measurements of \dot{P}_s . Pulsars B, G, H, K, and L exhibit many characteristics of black widow systems; Q and I are wider, circular MSP binaries; and N displays a significant eccentricity of $e = 0.093$ in a wide orbit of several days. Both Q and N have massive $M_c > 0.2 M_\odot$ companions, likely He white dwarfs.

Folding γ -ray photons from the *Fermi* LAT source associated with the cluster using the new radio ephemerides for G, H, and K yielded no detection of pulsed emission. From the non-detection of pulsed γ -ray emission from A–E, G, H, and K, we infer that none of these pulsars contributes more than 10% of the total γ -ray flux associated with the cluster. We identify *Chandra* X-ray sources 24f, 14c, 21d, and 32d (Henleywillis et al. 2018) as potential counterparts of G, H, K, and L, respectively. The folding

of *NICER* X-ray photons data yield no pulsed detections, and we place an upper limit of $5.3 \times 10^{-15} \text{ erg cm}^{-2} \text{ s}^{-1}$ on the X-ray flux from *XMM-Newton* observations (Gendre et al. 2003), consistent with previously reported values.

Measurements of \dot{P}_s are translated into constraints on the LOS accelerations of the pulsars from the cluster's acceleration field, which are consistent with a King-model gravitational potential given the cluster parameters. While these measurements are insensitive to a putative IMBH with mass 10^3 – $10^4 M_\odot$, they place an upper limit of $< 10^5 M_\odot$ at 90% confidence.

The total number of known MSPs in the cluster is broadly consistent with its γ -ray luminosity and total stellar encounter rate. The circular orbits of Q and I align with the low interaction rate per binary in the present-day cluster environment. However, the high fraction of isolated MSPs, the overabundance of black widow systems, and the eccentricity of N are difficult to reconcile with current encounter rate estimates. These findings indicate that present-day encounter rate parameters are not always reliable predictors of MSP populations. A significant fraction of the MSP population may therefore have formed in denser environments ($> 10^4 M_\odot \text{ pc}^{-3}$) than those observed today, consistent with the complex evolutionary history of ω Cen.

Acknowledgements. MCiB has been funded by the INAF Large Grant 2022 "GCjewels" (P.I. Andrea Possenti) approved with the Presidential Decree 30/2022. AP, FA, RN, AC, AC, and MB also benefited of the same "GCjewels" grant. AP was also supported in part by the "Italian Ministry of Foreign Affairs and International Cooperation", grant number ZA23GR03, under the project "RADIOMAP- Science and technology pathways to MeerKAT+: the Italian and South African synergy". This work was supported by the Regione Autonoma della Sardegna, under Regional Law n.7 of August 7, 2007 "Promozione della Ricerca Scientifica e dell'Innovazione Tecnologica in Sardegna" (Programma Mobilità Giovani Ricercatori, CUP: F74I19000180002). FA acknowledges that part of the research activities described in this paper were carried out with the contribution of the NextGenerationEU funds within the National Recovery and Resilience Plan (PNRR), Mission 4 – Education and Research, Component 2 – From Research to Business (M4C2), Investment Line 3.1 – Strengthening and creation of Research Infrastructures, Project IR0000034 – 'STILES - Strengthening the Italian Leadership in ELT and SKA'. VVK acknowledges continuing support from the Max Planck Society and financial support from the European Research Council (ERC) starting grant "COMPACT" (Grant agreement number 101078094). Work at NRL is supported by NASA. The MeerKAT telescope is operated by the South African Radio Astronomy Observatory (SARAO), which is a facility of the National Research Foundation, an agency of the Department of Science and Innovation. SARAO acknowledges the ongoing advice and calibration of GPS systems by the National Metrology Institute of South Africa (NMISA) and the time space reference systems department of the Paris Observatory. TRAPUM observations used the FBFUSE and APSUSE computing clusters for beamforming, data acquisition, storage and analysis. These instruments were funded, developed and installed by the Max-Planck-Institut für Radioastronomie and the Max-Planck Gesellschaft. Murriyang, CSIRO's Parkes radio telescope, is part of the Australia Telescope National Facility (<https://ror.org/05qajvd42>), which is funded by the Australian Government for operation as a National Facility managed by CSIRO. We acknowledge the Wiradjuri people as the Traditional Owners of the Observatory site. The INAF - OAC computer cluster used in this work has been acquired within a project aimed to enhance the Sardinia Radio Telescope (SRT). The Enhancement of the SRT for the study of the Universe at high radio frequencies is financially supported by the National Operative Program (Programma Operativo Nazionale - PON) of the Italian Ministry of University and Research "Research and Innovation 2014–2020", Notice D.D. 424 of 28/02/2018 for the granting of funding aimed at strengthening research infrastructures, in implementation of the Action II.1 - Project Proposal PIR01_00010. The *Fermi* LAT Collaboration acknowledges generous ongoing support from a number of agencies and institutes that have supported both the development and the operation of the LAT as well as scientific data analysis. These include the National Aeronautics and Space Administration and the Department of Energy in the United States, the Commissariat à l'Énergie Atomique and the Centre National de la Recherche Scientifique / Institut National de Physique Nucléaire et de Physique des Particules in France, the Agenzia Spaziale Italiana and the Istituto Nazionale di Fisica Nucleare in Italy, the Ministry of Education, Culture, Sports, Science and Technology (MEXT), High Energy Accelerator Research Organization (KEK) and Japan Aerospace Exploration Agency (JAXA) in Japan, and the K. A. Wallenberg Foundation, the Swedish Research Council and the Swedish National Space Board in Sweden. Additional support for science analysis during

the operations phase is gratefully acknowledged from the Istituto Nazionale di Astrofisica in Italy and the Centre National d'Études Spatiales in France. This work performed in part under DOE Contract DE-AC02-76SF00515. This work has made use of Singularity version 3.11. PRESTO and PSRCHIVE software used in this work were installed in Singularity containers provided by AR. This research makes use of the SciServer science platform (www.sciserver.org) for the analysis of the XMM observations. SciServer is a collaborative research environment for large-scale data-driven science. It is being developed at, and administered by, the Institute for Data Intensive Engineering and Science at Johns Hopkins University. SciServer is funded by the National Science Foundation through the Data Infrastructure Building Blocks (DIBBs) program and others, as well as by the Alfred P. Sloan Foundation and the Gordon and Betty Moore Foundation. This research has made use of data, software and/or web tools obtained from the High Energy Astrophysics Science Archive Research Center (HEASARC), a service of the Astrophysics Science Division at NASA/GSFC and of the Smithsonian Astrophysical Observatory's High Energy Astrophysics Division

References

- Abbate, F., Possenti, A., Ridolfi, A., et al. 2024, *MNRAS*, 532, 4089
- Abbate, F., Ridolfi, A., Barr, E. D., et al. 2022, *MNRAS*, 513, 2292
- Abdo, A. A., Ackermann, M., Ajello, M., et al. 2010, *A&A*, 524, A75
- Abdollahi, S., Acero, F., Baldini, L., et al. 2022, *ApJS*, 260, 53
- Andersen, B. C. & Ransom, S. M. 2018, *ApJ*, 863, L13
- Atwood, W., Albert, A., Baldini, L., et al. 2013, arXiv e-prints, arXiv:1303.3514
- Atwood, W. B., Abdo, A. A., Ackermann, M., et al. 2009, *ApJ*, 697, 1071
- Bañares-Hernández, A., Calore, F., Martin Camalich, J., & Read, J. I. 2025, *A&A*, 693, A104
- Bahramian, A., Heinke, C. O., Sivakoff, G. R., & Gladstone, J. C. 2013, *ApJ*, 766, 136
- Bailes, M., Jameson, A., Abbate, F., et al. 2020, *PASA*, 37, e028
- Ballet, J., Bruel, P., Burnett, T. H., Lott, B., & The Fermi-LAT collaboration. 2023, arXiv e-prints, arXiv:2307.12546
- Barr, E. D. 2018, in *IAU Symposium*, Vol. 337, Pulsar Astrophysics the Next Fifty Years, ed. P. Weltevrede, B. B. P. Perera, L. L. Preston, & S. Sanidas, 175–178
- Baumann, M., Boch, T., Pineau, F.-X., et al. 2022, in *Astronomical Society of the Pacific Conference Series*, Vol. 532, *Astronomical Data Analysis Software and Systems XXX*, ed. J. E. Ruiz, F. Pierfederici, & P. Teuben, 7
- Baumgardt, H. 2017, *MNRAS*, 464, 2174
- Baumgardt, H. & Hilker, M. 2018, *MNRAS*, 478, 1520
- Bekki, K. & Freeman, K. C. 2003, *MNRAS*, 346, L11
- Bellini, A., Milone, A. P., Anderson, J., et al. 2017, *ApJ*, 844, 164
- Benvenuto, O. G., De Vito, M. A., & Horvath, J. E. 2015, *MNRAS*, 449, 4184
- Bezuidenhout, M. C., Clark, C. J., Breton, R. P., et al. 2023, *RAS Techniques and Instruments*, 2, 114
- Bickel, P., Kleijn, B., & Rice, J. 2008, *ApJ*, 685, 384
- Blanchard, C., Guillemot, L., Voisin, G., Cognard, I., & Theureau, G. 2025, *A&A*, 698, A239
- Brown, A. M., Massey, R., Lacroix, T., et al. 2019, arXiv e-prints, arXiv:1907.08564
- Bruel, P., Burnett, T. H., Digel, S. W., et al. 2018, arXiv e-prints, arXiv:1810.11394
- Calamida, A., Zocchi, A., Bono, G., et al. 2020, *ApJ*, 891, 167
- Chen, H.-L., Chen, X., Tauris, T. M., & Han, Z. 2013, *ApJ*, 775, 27
- Chen, W., Barr, E., Karuppusamy, R., Kramer, M., & Stappers, B. 2021, *Journal of Astronomical Instrumentation*, 10, 2150013
- Chen, W., Freire, P. C. C., Ridolfi, A., et al. 2023, *MNRAS*, 520, 3847
- Clontz, C., Seth, A. C., Dotter, A., et al. 2024, *ApJ*, 977, 14
- Cool, A. M., Haggard, D., Arias, T., et al. 2013, *ApJ*, 763, 126
- Dai, S., Johnston, S., Kerr, M., et al. 2023, *MNRAS*, 521, 2616
- Dai, S., Johnston, S., Kerr, M., et al. 2020, *ApJ*, 888, L18
- Damour, T. & Deruelle, N. 1986, *Ann. Inst. Henri Poincaré Phys. Théor.*, 44, 263
- Damour, T. & Taylor, J. H. 1991, *ApJ*, 366, 501
- de Jager, O. C., Raubenheimer, B. C., & Swanepoel, J. W. H. 1989, *A&A*, 221, 180
- de Menezes, R. 2026, arXiv e-prints [arXiv:2602.20250]
- de Menezes, R., Cafardo, F., & Nemmen, R. 2019, *MNRAS*, 486, 851
- Dewey, R. J., Taylor, J. H., Weisberg, J. M., & Stokes, G. H. 1985, *ApJ*, 294, L25
- Dinescu, D. I., Girard, T. M., & van Altena, W. F. 1999, *AJ*, 117, 1792
- Dutta, A., Freire, P. C. C., Gautam, T., et al. 2025, *A&A*, 697, A166
- Evans, A. J., Strigari, L. E., & Zivick, P. 2022, *MNRAS*, 511, 4251
- Fahion, K., Lyubenova, M., van de Ven, G., et al. 2021, *A&A*, 650, A137
- Freire, P. C., Kramer, M., & Lyne, A. G. 2001, *MNRAS*, 322, 885
- Freire, P. C. C., Abdo, A. A., Ajello, M., et al. 2011, *Science*, 334, 1107
- Freire, P. C. C., Hessels, J. W. T., Nice, D. J., et al. 2005, *ApJ*, 621, 959
- Freire, P. C. C. & Ridolfi, A. 2018, *MNRAS*, 476, 4794
- Freire, P. C. C., Ridolfi, A., Kramer, M., et al. 2017, *MNRAS*, 471, 857
- Fruchter, A. S., Stinebring, D. R., & Taylor, J. H. 1988, *Nature*, 333, 237
- Gaia Collaboration, Helmi, A., van Leeuwen, F., et al. 2018, *A&A*, 616, A12
- Gendre, B., Barret, D., & Webb, N. A. 2003, *A&A*, 400, 521
- Gendreau, K. C., Arzoumanian, Z., & Okajima, T. 2012, in *Society of Photo-Optical Instrumentation Engineers (SPIE) Conference Series*, Vol. 8443, *Space Telescopes and Instrumentation 2012: Ultraviolet to Gamma Ray*, ed. T. Takahashi, S. S. Murray, & J.-W. A. den Herder, 844313
- Grunthal, K., Venkatraman Krishnan, V., Freire, P. C. C., et al. 2024, *A&A*, 691, A22
- Guo, Y., Wang, B., & Han, Z. 2022, *MNRAS*, 515, 2725
- Häberle, M., Neumayer, N., Clontz, C., et al. 2025, *ApJ*, 983, 95
- Häberle, M., Neumayer, N., Seth, A., et al. 2024, *Nature*, 631, 285
- Harris, W. E. 2010, arXiv e-prints [arXiv:1012.3224]
- Heggie, D. C. 1975, *MNRAS*, 173, 729
- Henleywillis, S., Cool, A. M., Haggard, D., et al. 2018, *MNRAS*, 479, 2834
- Hilker, M. & Richtler, T. 2000, *A&A*, 362, 895
- Hills, J. G. 1975, *AJ*, 80, 809
- Hobbs, G., Manchester, R. N., Dunning, A., et al. 2020, *PASA*, 37, e012
- Hobbs, G. B., Edwards, R. T., & Manchester, R. N. 2006, *MNRAS*, 369, 655
- Hotan, A. W., van Straten, W., & Manchester, R. N. 2004, *PASA*, 21, 302
- Hui, C. Y., Cheng, K. S., & Taam, R. E. 2010, *ApJ*, 714, 1149
- Ibata, R. A., Bellazzini, M., Malhan, K., Martin, N., & Bianchini, P. 2019, *Nature Astronomy*, 3, 667
- Jalali, B., Baumgardt, H., Kissler-Patig, M., et al. 2012, *A&A*, 538, A19
- Kerr, M. 2011, *ApJ*, 732, 38
- King, A. R., Davies, M. B., & Beer, M. E. 2003, *MNRAS*, 345, 678
- King, I. 1962, *AJ*, 67, 471
- Lange, C., Camilo, F., Wex, N., et al. 2001, *MNRAS*, 326, 274
- Lee, Y. W., Joo, J. M., Sohn, Y. J., et al. 1999, *Nature*, 402, 55
- Limberg, G., Souza, S. O., Pérez-Villegas, A., et al. 2022, *ApJ*, 935, 109
- Luo, J., Ransom, S., Demorest, P., et al. 2021, *ApJ*, 911, 45
- Majewski, S. R., Nidever, D. L., Smith, V. V., et al. 2012, *ApJ*, 747, L37
- Manchester, R. N., Hobbs, G. B., Teoh, A., & Hobbs, M. 2005, *AJ*, 129, 1993
- Massari, D., Koppelman, H. H., & Helmi, A. 2019, *A&A*, 630, L4
- McConnell, D., Deshpande, A. A., Connors, T., & Ables, J. G. 2004, *MNRAS*, 348, 1409
- McMillan, P. J. 2017, *MNRAS*, 465, 76
- Morello, V., Barr, E. D., Cooper, S., et al. 2019, *MNRAS*, 483, 3673
- Morello, V., Barr, E. D., Stappers, B. W., Keane, E. F., & Lyne, A. G. 2020, *MNRAS*, 497, 4654
- Myeong, G. C., Vasiliev, E., Iorio, G., Evans, N. W., & Belokurov, V. 2019, *MNRAS*, 488, 1235
- Neumayer, N., Seth, A., & Böker, T. 2020, *A&A Rev.*, 28, 4
- Nice, D., Demorest, P., Stairs, I., et al. 2015, *Tempo: Pulsar timing data analysis, Astrophysics Source Code Library, record ascl:1509.002*
- Nitschai, M. S., Neumayer, N., Häberle, M., et al. 2024, *ApJ*, 970, 152
- Noyola, E., Gebhardt, K., & Bergmann, M. 2008, *ApJ*, 676, 1008
- Noyola, E., Gebhardt, K., Kissler-Patig, M., et al. 2010, *ApJ*, 719, L60
- Padmanabh, P. V., Barr, E. D., Sridhar, S. S., et al. 2023, *MNRAS*, 524, 1291
- Padmanabh, P. V., Ransom, S. M., Freire, P. C. C., et al. 2024, *A&A*, 686, A166
- Pagnini, G., Di Matteo, P., Hayward, M., et al. 2025, *A&A*, 693, A155
- Pfeffer, J., Lardo, C., Bastian, N., Saracino, S., & Kamann, S. 2021, *MNRAS*, 500, 2514
- Prager, B. J., Ransom, S. M., Freire, P. C. C., et al. 2017, *ApJ*, 845, 148
- Ransom, S. M., Eikenberry, S. S., & Middleditch, J. 2002, *AJ*, 124, 1788
- Rasio, F. A. & Heggie, D. C. 1995, *ApJ*, 445, L133
- Ray, P. S., Kerr, M., Parent, D., et al. 2011, *ApJS*, 194, 17
- Reynoso-Cordova, J., Burgueño, O., Geringer-Sameth, A., et al. 2021, *J. Cosmology Astropart. Phys.*, 2021, 010
- Ridolfi, A., Gautam, T., Freire, P. C. C., et al. 2021, *MNRAS*, 504, 1407
- Roberts, M. S. E. 2013, in *Proceedings of the IAU Symposium*, Vol. 291, *Neutron Stars and Pulsars: Challenges and Opportunities after 80 Years*, ed. J. van Leeuwen (Cambridge: Cambridge University Press), 127
- Rutledge, R. E., Bildsten, L., Brown, E. F., Pavlov, G. G., & Zavlin, V. E. 2002, *ApJ*, 578, 405
- Shaifullah, G., Verbiest, J. P. W., Freire, P. C. C., et al. 2016, *MNRAS*, 462, 1029
- Shklovskii, I. S. 1970, *Soviet Ast.*, 13, 562
- Smith, D. A., Abdollahi, S., Ajello, M., et al. 2023, *ApJ*, 958, 191
- Sollima, A., Ferraro, F. R., & Bellazzini, M. 2007, *MNRAS*, 381, 1575
- Stappers, B. & Kramer, M. 2016, in *MeerKAT Science: On the Pathway to the SKA*, 9
- Tailo, M., Di Criscienzo, M., D'Antona, F., Caloi, V., & Ventura, P. 2016, *MNRAS*, 457, 4525
- Tauris, T. M. & Savonije, G. J. 1999, *A&A*, 350, 928
- Taylor, M. B. 2005, in *Astronomical Society of the Pacific Conference Series*, Vol. 347, *Astronomical Data Analysis Software and Systems XIV*, ed. P. Shopbell, M. Britton, & R. Ebert, 29
- van den Heuvel, E. P. J. & van Paradijs, J. 1988, *Nature*, 334, 227
- van der Marel, R. P. & Anderson, J. 2010, *ApJ*, 710, 1063
- van Straten, W. & Bailes, M. 2011, *PASA*, 28, 1
- Verbunt, F. & Freire, P. C. C. 2014, *A&A*, 561, A11
- Verbunt, F. & Hut, P. 1987, in *IAU Symposium*, Vol. 125, *The Origin and Evolution of Neutron Stars*, ed. D. J. Helfand & J.-H. Huang, 187
- Villanova, S., Geisler, D., Gratton, R. G., & Cassisi, S. 2014, *ApJ*, 791, 107
- Vleeschouwer, L., Corongiu, A., Stappers, B. W., et al. 2024, *MNRAS*, 530, 1436
- Wu, Y., Pan, Z., Qian, L., et al. 2024, *ApJ*, 974, L23
- Yin, D., Zhang, L.-y., Qian, L., et al. 2024, *ApJ*, 969, L7
- Zhao, J. & Heinke, C. O. 2022, *MNRAS*, 511, 5964
- Zocchi, A., Gieles, M., & Hénault-Brunet, V. 2017, *MNRAS*, 468, 4429
- Zocchi, A., Gieles, M., & Hénault-Brunet, V. 2019, *MNRAS*, 482, 4713

Appendix A: Details about MeerKAT observations

Table A.1: Summary of MeerKAT APSUSE observations used in this work.

Date	Project	Receiver	Duration (hours)	Sampling (μ s)	Array	Tiling	Comments
2021-03-21	TRAPUM	L-band	3.8	153.121	Core	M, A, P	Searched in (Chen et al. 2023)
2021-03-26	TRAPUM	L-band	3.7	153.121	Core	M, A, P	Searched in (Chen et al. 2023)
2023-06-27	MeerTIME	L-band	4.0	76.5607	Full	A, Pm	Follow-up
2023-08-20	MeerTIME	L-band	4.0	76.5607	Full	A, Pm	Follow-up
2023-10-05	MeerTIME	L-band	4.0	76.5607	Full	A, Pm	All beams corrupted, data not used
2024-01-21	MeerTIME	S-band	2.0	18.7246	Full	A, Pm	Part of S-band GC survey (Nag et al., in prep.)
2024-01-22	MeerTIME	S-band	2.0	18.7246	Full	A, Pm	Starts at the end of previous, 4 hours total
2024-02-12	MeerTIME	S-band	2.0	74.8983	Full	A, Pm	Some beams lost, > 2.7 GHz sub-band lost
2025-02-11	TRAPUM	UHF	3.0	120.471	Core	M(0.7), A, Pm	Searched in this work
2025-07-28	TRAPUM	UHF	3.0	240.941	Full	M(0.7), A, Pm	> 0.95 GHz sub-band lost

Notes. PTUSE observation from 14 February, 2024 is not included, as it was only used for pulsar L. Core array: inner 44 antennas. Full array: 55+ antennas. Receiver frequency coverages: L-band (856–1712 MHz), S-band (S1 configuration, 1968–2843 MHz, Barr 2018), and UHF (544–1088 MHz). M: MOSAIC coherent beam tiling (0.7: defined beam overlap, if set). A: coherent beams on ATCA sources (Dai et al. 2023). P: coherent beams on locations of pulsars A and B (Dai et al. 2023). Pm: coherent beams on locations of all Parkes and MeerKAT pulsar discoveries (Dai et al. 2023; Chen et al. 2023).

MeerKAT observations were processed on the Filterbanking Beamformer User Supplied Equipment (FBFUSE) cluster for beamforming, and were subsequently stored as search-mode filterbanks (without coherent de-dispersion) in the Accelerated Pulsar Search User Supplied Equipment (APSUSE) (see Barr 2018; Padmanabh et al. 2023).

The observations are listed in Table A.1. All observing sessions lasted between three and four hours. The 21 and 27 April 2021 observations, as well as the 11 February 2025 observation, implemented full coherent beam tilings derived with MOSAIC (Chen et al. 2021), with additional coherent beams implemented on optimal pulsar and ATCA²¹ source positions as reported by Dai et al. (2023) and Chen et al. (2023). The remaining observations only implemented individual beams on pulsar positions. The 12 February 2024 and 28 July 2025 observations suffered partial recording failures, resulting in the loss of a fraction of the observing band in both cases; additionally, during the 12 February 2024 observation, a subset of beams was corrupted and lost entirely. Nevertheless, the remaining usable bandwidth and beams were retained and used in the scientific analysis presented in this work.

²¹ <https://www.narrabri.atnf.csiro.au/>

Appendix B: Sky coverage and sensitivity of TRAPUM searches

The sensitivity of our search was approximately 20 μJy , which, following Chen et al. (2023), was estimated using the radiometer equation (Dewey et al. 1985),

$$S_{\min} = \frac{S/N \beta T_{\text{sys}}}{\varepsilon_{\text{FFT}} G \sqrt{n_{\text{pol}} \Delta F \Delta t}} \sqrt{\frac{\zeta}{1-\zeta}}. \quad (\text{B.1})$$

Here, $S/N = 10$ is the minimum detection signal-to-noise ratio; $\beta = 1.01$ is the digitization correction factor; $T_{\text{sys}} = 36$ K is the system temperature, including contributions from the sky at UHF (5.5 K), spillover and atmosphere (6.5 K), and the receiver (24 K)²²; $\varepsilon_{\text{FFT}} = 0.07$ is the FFT efficiency (Morello et al. 2020); $G = 1.92$ K Jy^{-1} for the core array (44 antennas) is the combined MeerKAT antenna gain; $n_{\text{p}} = 2$ is the number of summed polarisations; $\Delta f = 500$ MHz is the effective bandwidth after radio-frequency interference (RFI) excision; $\Delta t = 3$ h is the integration time and $\zeta = 0.1$ is the assumed pulse duty cycle at UHF.

All ATCA beams from the 21 March 2021 observation have been searched. The search for pulsars in the 11 February 2025 observation is an ongoing effort: 56 out of 283 have been searched, and the resulting pulsar candidates have been inspected. This covers most of the core region of ω Cen. Figure B.1 shows the MOSAIC coherent beam tiling of the 11 February 2025 observation and the searched beams.

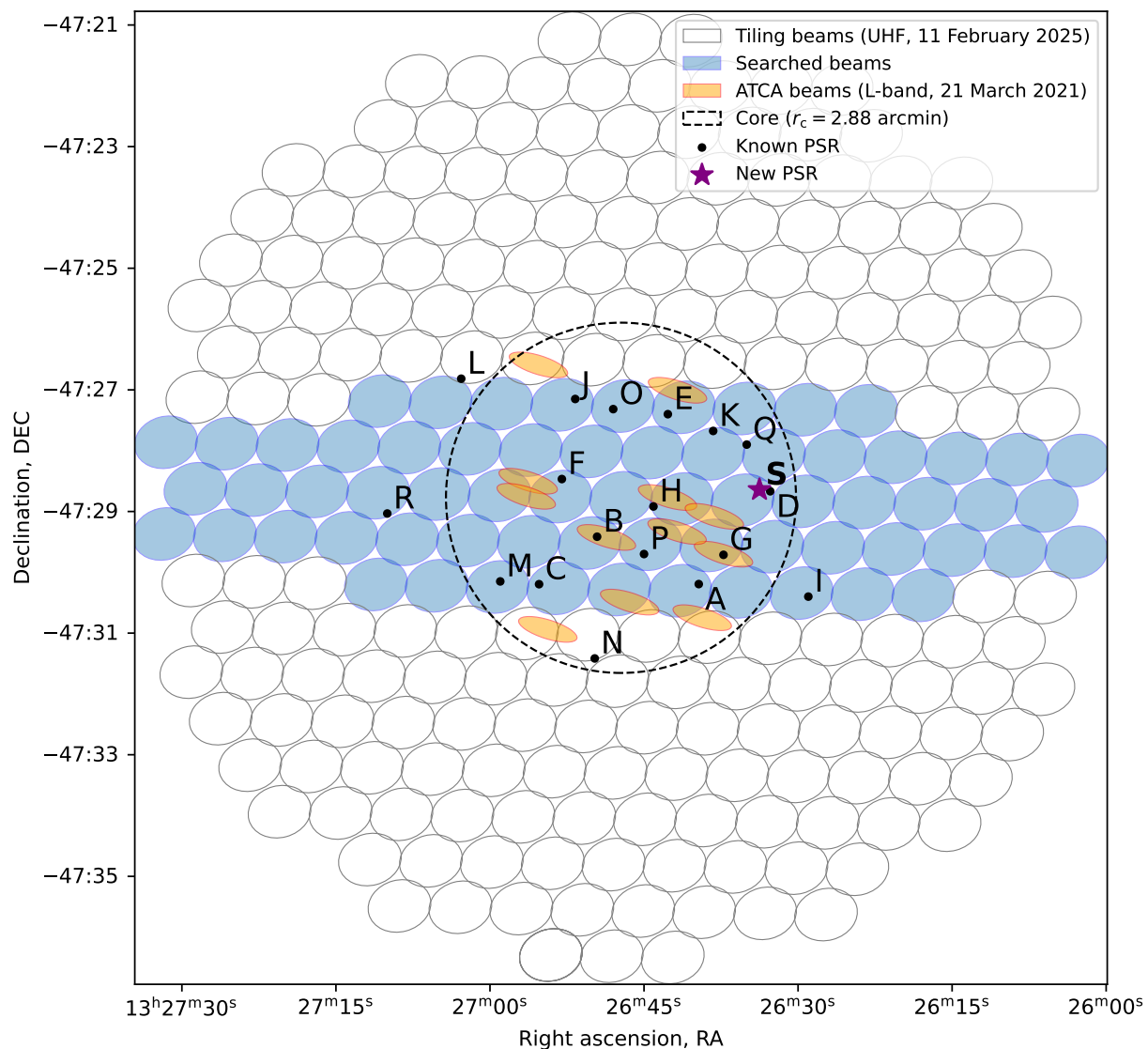


Fig. B.1: Beams included in the pulsar searches discussed in this work, centered on the optical center of ω Cen. The beams correspond to the MOSAIC coherent beam tiling generated for the 11 February 2025 observation (searched beams highlighted with solid colors) and to the ATCA beams from the 21 March 2021 observation. The ω Cen core radius, as reported by Baumgardt & Hilker (2018), is also shown. Previously known pulsars are indicated, with positions derived from timing or as reported by Chen et al. (2023). Our new UHF discovery, S, is also highlighted at its localized position with a star symbol.

²² <https://skaafrika.atlassian.net/wiki/spaces/ESDKB/pages/277315585/MeerKAT+specifications>

Appendix C: Derivation of orbital and timing solutions

C.1. Orbital solutions

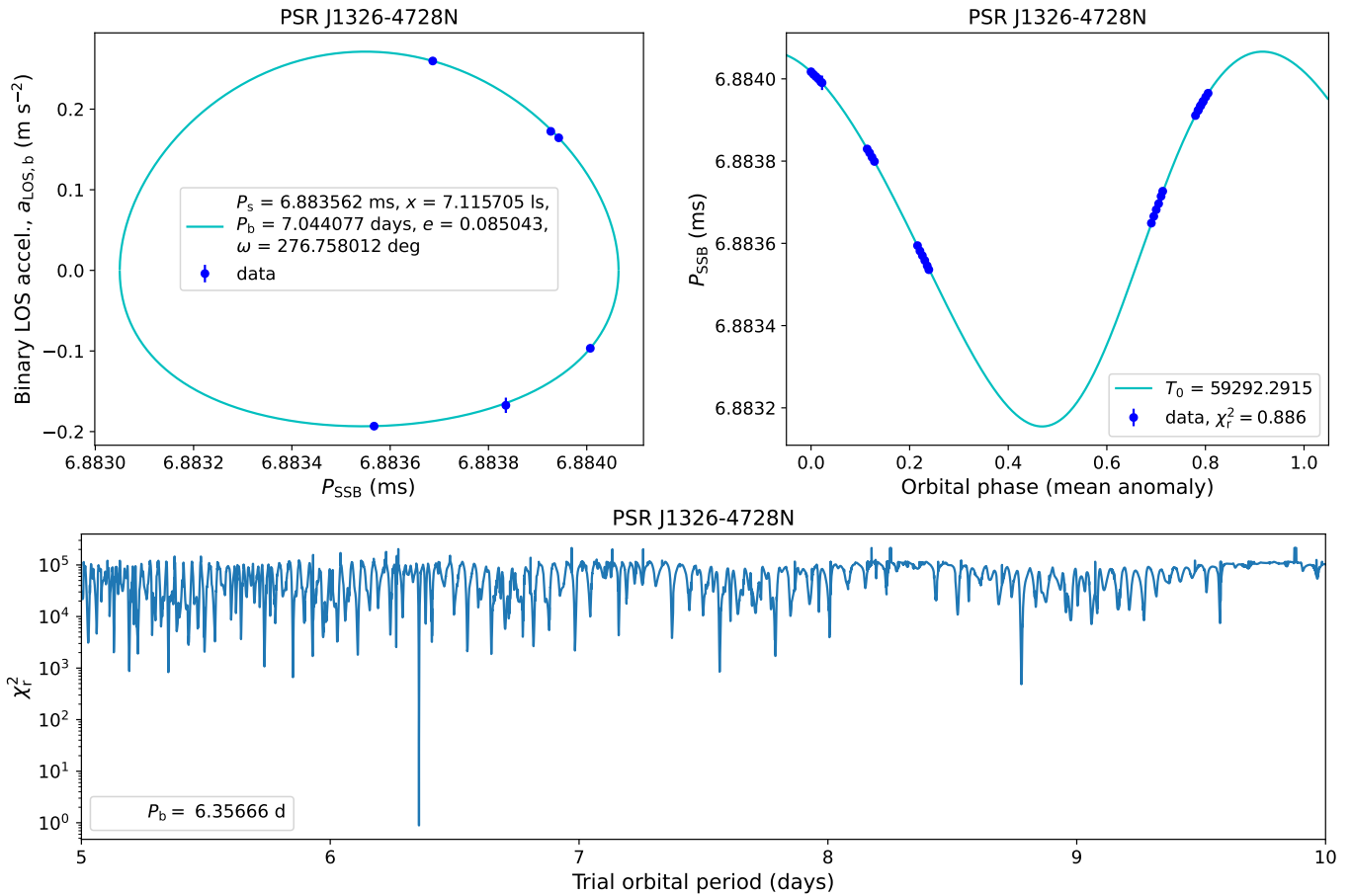


Fig. C.1: Keplerian orbital fits to the P_{SSB} and $a_{\text{LOS},b}$ measurements of N. Top left: successful fit of the curve traced in the $P_{\text{SSB}}-a_{\text{LOS},b}$ plane by a general Keplerian orbit, providing approximate orbital parameters. Top right: successful fit to the P_{SSB} –orbital phase, folded at the orbital period. Bottom: quality of the Keplerian fits, expressed as the reduced χ^2 computed from the fit residuals and uncertainties, across a range of trial orbital periods. Each point corresponds to a general Keplerian fit performed at a given trial period. All plots were generated with our custom code for fitting Keplerian orbits (https://github.com/mcbernadich/pulsar_orbit_solver)

Before proceeding to pulsar timing, we refined the Keplerian orbital solutions for the ω Cen binary pulsars discovered by Chen et al. (2023): G, H, I, K, L, N, and Q. This refinement was necessary to obtain accurate, orbitally coherent folding solutions suitable for subsequent timing analyses with both the MeerKAT and Murriyang UWL data sets.

The updated orbital solutions were derived using the MeerKAT data set (Table 2.2), owing to the telescope’s higher sensitivity. We performed direct refolding or periodicity searches on coherent beams placed at the position of each pulsar in the 27 June and 20 August 2023 observations, as well as in the 11 February and 28 July 2025 observations, in order to obtain high signal-to-noise detections. Reasonable detections of G, H, K, and L were achieved through direct refolding of the sub-banded filterbanks into pulsar archives using `dspsr`²³ (van Straten & Bailes 2011) and the orbital solutions reported by Chen et al. (2023). By contrast, I, N, and Q required additional periodicity searches in their corresponding beams. These searches were carried out using PRESTO’s `accelesearch`, yielding significant detections in all observations except for Q in the 28 July 2025 observation.

Once reliable detections had been obtained, we refined the orbital solutions. First, the pulsar archives were cleaned of radio-frequency interference using `clfd`, an outlier-detection algorithm (Morello et al. 2019). We then measured the optimal spin periods at the solar-system barycentre (SSB), P_{SSB} , and the apparent LOS accelerations due to binary motion, $a_{\text{LOS},b}$, using PSRCHIVE’s²⁴ (Hotan et al. 2004) `pdmp`²⁵. These measurements were performed on segments of each observation. The resulting P_{SSB} values were subsequently fitted with Keplerian models describing their evolution over time with a custom code developed for general orbital periodicity searches and Keplerian orbital modelling²⁶.

²³ <https://github.com/demorest/dspsr>

²⁴ <https://psrchive.sourceforge.net/>

²⁵ <https://psrchive.sourceforge.net/manuals/pdmp/>

²⁶ https://github.com/mcbernadich/pulsar_orbit_solver

For G, H, K, and L, this procedure was straightforward, owing to the reliable orbital solutions reported by Chen et al. (2023). In contrast, I, N, and Q required more elaborate solving strategies. For these systems, we first obtained preliminary Keplerian parameters (orbital period P_b , projected semi-major axis x , and eccentricity parameters e and ω) by fitting the curve traced by the orbit in the $P_{\text{SSB}}-a_{\text{LOS,b}}$ plane for the first estimation of approximate, preliminary orbital parameters (see the top-left panel of Figure C.1 for N; for a detailed description of this method, see Freire et al. 2001). Using these parameters as priors, we then searched for the true orbital period by fitting Keplerian models (including the time of periastron, T_0) to the P_{SSB} time series over a grid of trial P_b values. The optimal orbital period was identified as the solution yielding the minimum reduced χ^2 (bottom panel of Figure C.1). This step was crucial for achieving orbital coherence between observations separated by many months. Finally, fixing P_b to this optimal value, we performed a full Keplerian fit to the P_{SSB} time series to obtain the final folding solution (top-right panel of Figure C.1).

The obtained orbital solutions, together with the spin periods of isolated pulsars discovered in Chen et al. (2023), enabled us to search for additional detections in the Murriyang UWL observations through direct folding. Using this approach, we obtained frequent, moderate signal-to-noise detections of G, H, I, and K; occasional low signal-to-noise detections of J and O; and no significant detections of F, L, M, N, P, Q, R, and S. This latter set of pulsars was already among the faintest MeerKAT discoveries in Cen, making their non-detection with Murriyang UWL unsurprising.

We also folded the MeerKAT S-band observations, achieving high signal-to-noise detections of G and K, as well as low signal-to-noise detections of I, L, and N. Q also remained undetected in the 28 July 2025 MeerKAT UHF observation. This non-detection can be explained by a combination of three factors: its intrinsically faint nature, the presence of significant scattering at $f < 1$ GHz, and the loss of the $f > 0.95$ GHz sub-band due to a recording failure (see Table A.1 and Appendix A).

C.2. Timing solutions

Phase-connected timing solutions were searched jointly with MeerKAT and Murriyang UWL observations for pulsars that were detectable with both telescopes. The folded pulsar archives from the MeerKAT observations were first cleaned of RFI using `c1fd` and then integrated in frequency. Times of arrival (ToAs) were derived every few minutes in each observation where the pulsars were detected, using PSRCHIVE's `pat`, and high signal-to-noise detections from MeerKAT observations from 2023 were used as timing templates. For MeerKAT, multiple frequency-integrated ToA were obtained per observation, including from the S-band if detectable. The folded Murriyang UWL observations were calibrated using the polarisation calibrator files, cleaned of RFI with `c1fd`, and manually inspected with `pazi` to remove any remaining contaminated channels or sub-integrations. The lower frequency band ($f < 2368$ MHz) was integrated across frequency and polarisation.

To ensure the reliability of multiple time-resolve ToAs from Murriyang UWL, we selected only observations with clear detections and low-uncertainty ToAs. These were then combined with the MeerKAT-derived ToAs, implementing a global jump between the two telescopes, to search for phase-connected timing solutions using `dracula`²⁷, a phase-connection algorithm that explores all possible phase-turn combinations between observations to identify a unique solution (Freire & Ridolfi 2018). The fits were performed with the pulsar timing software `Tempo`²⁸ (Nice et al. 2015), and they included spin frequency ν and its derivative $\dot{\nu}$, Keplerian orbital parameters for binaries, and the position parameters RA and DEC.

Phase-connected timing solutions were obtained for G, H, and K, spanning both telescopes from 2020 to 2025. A single unambiguous solution was not achieved for I, J, and O. For J and O, this is explained by the limited availability of usable Murriyang UWL detections due to their intrinsic faintness, which either forced inclusion of unreliable ToAs or removal of too many ToAs during processing. Pulsar I, though brighter and more frequently detected, likely failed due to (i) its very wide profile, causing large ToA uncertainties, (ii) its longer orbital period, complicating phase connection, and (iii) unidentified unreliable ToAs from the Murriyang UWL data.

²⁷ <https://github.com/pfreire163/Dracula>

²⁸ <https://tempo.sourceforge.net/>

Appendix D: Full timing parameters tables

We list the full timing parameters from our timing and orbital solutions in the tables below. Table D.1 lists the timing parameters of pulsars A, C, D, and E, which are isolated. Table D.2 lists the timing parameters of pulsars B, G, H, and K, which are in binaries. Table D.3 lists the timing parameters from the jumped timing solutions (orbital solutions) for binary pulsars I, L, N, and Q.

Table D.1: Data reduction, spin, astrometric, and derived parameters from timing solutions for isolated pulsars A, C, D, and E. Derived from the fits shown in Figure 3. Spin and astrometric parameters: right ascension, declination, proper motion in RA, proper motion in DEC, spin frequency, spin frequency derivative, second spin frequency derivative, dispersion measure, dispersion measure derivative, epoch of DM and ν , and parallax (fixed). Derived parameters: spin period, observed spin period derivative, Shklovskii contribution to spin period derivative, Galactic relative line-of-sight acceleration contribution to the spin period derivative, and cluster line-of-sight acceleration.

PSR	J1326–4728A	J1326–4728C	J1326–4728D	J1326–4728E
ToA integration time (mins)				
MeerKAT L-band	...	51.2	51.2	...
MeerKAT S-band	...	102.4	102.4	...
MeerKAT UHF	...	51.2	51.2	...
Murriyang UWL	full	full	full	full
Data reduction parameters				
Ephemeris	DE430	DE430	DE430	DE430
Timescale	TDB	TCB	TCB	TCB
MeerKAT EFAC	...	1.6	1.5	...
UWL EFAC	1.0	1.0	1.0	1.0
RMS (μ s)	6.17	25.5	18.2	7.63
χ^2_r	1.2229	1.2784	1.3053	0.9692
Spin and astrometric parameters				
RA (J2000)	13 ^h 26 ^m 39.66801(5) ^s	13 ^h 26 ^m 55.22006(15) ^s	13 ^h 26 ^m 32.71198(10) ^s	13 ^h 26 ^m 42.67713(5) ^s
DEC (J2000)	–47:30:11.6683(6)	–47:30:11.772(2)	–47:28:40.0734(17)	–47:27:24.0234(8)
μ_{RA} (mas yr ^{–1})	–3.9 ± 0.3	–6.0 ± 1.1	–4.0 ± 0.8	–4.2 ± 0.4
μ_{DEC} (mas yr ^{–1})	–6.7 ± 0.6	–13.0 ± 1.8	–9.4 ± 1.3	–7.5 ± 0.6
ν (Hz)	243.380883764925(10)	145.60577015456(2)	218.39623733272(2)	237.658566377294(13)
$\dot{\nu}$ (Hz s ^{–1})	–1.61892(16) × 10 ^{–15}	–2.149(3) × 10 ^{–16}	1.9644(3) × 10 ^{–15}	–9.1866(19) × 10 ^{–16}
$\ddot{\nu}$ (Hz s ^{–2})	5.7 ± 1.0 × 10 ^{–26}	8.9 ± 2.3 × 10 ^{–26}	3.8 ± 2.5 × 10 ^{–26}	2.3 ± 1.3 × 10 ^{–26}
DM ₀ (pc cm ^{–3})	100.3267(4)	100.6643(13)	96.5462(9)	94.33967(5)
DM ₁ (pc cm ^{–3} yr ^{–1})	2.3 ± 0.3 × 10 ^{–3}	1.7 ± 0.8 × 10 ^{–5}	2.0 ± 5.6 × 10 ^{–4}	5.9 ± 3.5 × 10 ^{–3}
Epoch (MJD)	59923	59923	59923	59923
PX (mas)	0.913	0.913	0.913	0.913
Derived parameters				
P_s (ms)	4.10878613197030(16)	6.8678596935996(10)	4.5788334644086(5)	4.2077170423236(2)
\dot{P}_s (s s ^{–1})	2.7331(3) × 10 ^{–20}	1.0136(15) × 10 ^{–20}	–4.1184(7) × 10 ^{–20}	1.6265(3) × 10 ^{–20}
\dot{P}_{Sh}	1.62 × 10 ^{–21}	1.88 × 10 ^{–21}	7.56 × 10 ^{–21}	4.17 × 10 ^{–21}
\dot{P}_G	–1.42 × 10 ^{–21}	–2.38 × 10 ^{–21}	–1.59 × 10 ^{–21}	–1.46 × 10 ^{–21}
$a_{LOS,c}$ (m s ^{–2})	< 1.98(11) × 10 ^{–9}	< –2.75 ± 13.6 × 10 ^{–10}	< –3.09(70) × 10 ^{–9}	< 9.66(45) × 10 ^{–10}

Notes. ToA integration times may be larger than indicated due to PSRCHIVE rounding up when the last subintegration is too short. To mitigate scattering effects, only Murriyang UWL ToAs are included for pulsars A and E.

Table D.2: Data reduction, spin, astrometric, orbital, and derived parameters from timing solutions for binary pulsars B, G, H, and K. Derived from the fits shown in Figure 3. Spin and astrometric parameters: right ascension, declination, proper motion in RA, proper motion in DEC, spin frequency, spin frequency derivative, second spin frequency derivative, dispersion measure, dispersion measure derivative, epoch of DM and ν , and parallax (fixed). Orbital parameters: orbital period, orbital period derivative, projected semi-major axis, time of ascending node, eccentricity parameter 1, eccentricity parameter 2. Derived parameters: spin period, observed spin period derivative, Shklovskii contribution to spin period derivative, Galactic relative line-of-sight acceleration contribution to the spin period derivative, cluster line-of-sight acceleration, companion mass.

PSR	J1326–4728B	J1326–4728G	J1326–4728H	J1326–4728K
ToA integration time (mins)				
MeerKAT L-band	12.8	25.6	51.2	12.8
MeerKAT S-band	12.8	25.6	102.4	25.6
MeerKAT UHF	12.8	25.6	...	12.8
Murriyang UWL	30.0	30.0	60.0	30.0
Data reduction parameters				
Binary model	ELL1	ELL1	ELL1	ELL1
Ephemeris	DE430	DE430	DE430	DE430
Timescale	TCB	TDB	TDB	TDB
MeerKAT EFAC	2.0	1.7	1.0	1.3
UWL EFAC	2.0	1.5	1.0	1.2
RMS (μ s)	25.8	36.9	10.8	22.2
χ^2_r	1.2927	1.2986	1.1900	1.2005
Spin and astrometric parameters				
RA (J2000)	13 ^h 26 ^m 49.56786(7) ^s	13 ^h 26 ^m 37.26294(11) ^s	13 ^h 26 ^m 44.08336(6) ^s	13 ^h 26 ^m 38.26692(11) ^s
DEC (J2000)	−47:29:24.9136(11)	−47:29:42.7703(18)	−47:28:55.0721(8)	−47:27:40.5416(15)
μ_{RA} (mas yr ^{−1})	−2.8 ± 0.6	−2.8 ± 0.9	−3.7 ± 0.4	−3.8 ± 0.8
μ_{DEC} (mas yr ^{−1})	−11.4 ± 0.9	−8.2 ± 1.3	−7.4 ± 0.6	−7.0 ± 1.1
ν (Hz)	208.686833369112(14)	302.62833583619(3)	396.75803057690(2)	212.052884295491(18)
$\dot{\nu}$ (Hz s ^{−1})	$2.3663(3) \times 10^{-15}$	$-2.5404(5) \times 10^{-15}$	$-6.2768(3) \times 10^{15}$	$4.085(3) \times 10^{-16}$
$\ddot{\nu}$ (Hz s ^{−1})	$8.8 \pm 1.7 \times 10^{-26}$	$1.5 \pm 3.7 \times 10^{-26}$	$8.8 \pm 2.2 \times 10^{-26}$	$9.6 \pm 2.2 \times 10^{-26}$
DM ₀ (pc cm ^{−3})	100.2806(8)	99.7445(10)	98.1716(5)	94.7836(7)
DM ₁ (pc cm ^{−3} yr ^{−1})	$6.8 \pm 5.4 \times 10^{-4}$	$-8.7 \pm 6.4 \times 10^{-4}$	$-1.5 \pm 0.4 \times 10^{-3}$	$-5.8 \pm 4.4 \times 10^{-4}$
Epoch (MJD)	59923	59923	59923	59923
PX (mas)	0.913	0.913	0.913	0.913
Orbital parameters				
P_b (days)	0.08961120448(18)	0.1087595214(2)	0.1356937596(2)	0.09387146188(6)
\dot{P}_b (s s ^{−1})	$2.8 \pm 0.7 \times 10^{-12}$	$1.6 \pm 0.8 \times 10^{-12}$	$-2.0 \pm 0.8 \times 10^{-12}$	$6.25 \pm 0.19 \times 10^{-12}$
x (ls)	0.0214545(13)	0.032208(2)	0.0218759(10)	0.067954(2)
T_A (MJD)	59923.1256591(11)	59923.4072441(15)	59923.7583413(15)	59923.7255451(4)
η	$-6.2(\pm 11.8) \times 10^{-5}$	$5.4(\pm 1.3) \times 10^{-4}$	$2.7(\pm 9.3) \times 10^{-5}$	$1.0(\pm 0.5) \times 10^{-4}$
κ	$-4.9(\pm 1.2) \times 10^{-4}$	$-3.9(1.3) \times 10^{-4}$	$-1.3(\pm 0.8) \times 10^{-4}$	$-6.6(\pm 4.1) \times 10^{-5}$
Derived parameters				
P_s (ms)	4.7918691555938(3)	3.3043832370717(3)	2.52042787526183(13)	4.7158047546598(4)
\dot{P}_s (s s ^{−1})	$-5.4336(6) \times 10^{-20}$	$2.7739(5) \times 10^{-20}$	$3.9874(2) \times 10^{-20}$	$-9.0847(7) \times 10^{-21}$
\dot{P}_{Sh}	8.81×10^{-21}	3.31×10^{-21}	2.88×10^{-21}	4.00×10^{-21}
\dot{P}_G	-1.66×10^{-21}	-1.14×10^{-21}	-8.73×10^{-21}	-1.63×10^{-21}
$a_{LOS,c}$ (m s ^{−2})	$< -3.85 \pm 1.0 \times 10^{-9}$	$< 2.32(54) \times 10^{-9}$	$< 4.58(43) \times 10^{-9}$	$< -7.28(40) \times 10^{-10}$
M_c (M_\odot)	> 0.013	> 0.018	> 0.010	> 0.042

Notes. ToA integration times may be larger than indicated due to PSRCHIVE rounding up when the last subintegration is too short. To mitigate scattering effects, only MeerKAT ToAs at radio frequency higher than 1.4 GHz are included for J1326–4728H. Minimum companion mass derived from the mass function and assuming a pulsar mass of $M_p = 1.35 M_\odot$ and an inclination angle of $i = 90^\circ$.

Table D.3: Data reduction, spin, astrometric, orbital, and derived parameters from orbital solutions for I, L, N, and Q. Derived from the fits shown in Figure 4. Spin and astrometric parameters: right ascension, declination, spin frequency derivative, dispersion measure. Orbital parameters: orbital period, projected semi-major axis, time of ascending node, eccentricity parameter 1, eccentricity parameter 2, time of passage of periastron, eccentricity, angle of periastron. Derived parameters: spin period, companion mass.

PSR	J1326–4728I	J1326–4728L	J1326–4728N	J1326–4728Q
Data reduction parameters				
Data set	MeerKAT	MeerKAT	MeerKAT	MeerKAT
Binary model	ELL1	ELL1	DD	ELL1
Ephemeris	DE430	DE430	DE430	DE430
Timescale	TDB	TDB	TDB	TDB
RMS (μ s)	83.2	33.2	23.3	31.4
χ_r^2	0.8360	1.3777	1.3181	0.8345
Spin and astrometric parameters				
RA (J2000)	13 ^h 26 ^m 29.0 ^s	13 ^h 27 ^m 02.8 ^s	13 ^h 26 ^m 49.8 ^s	13 ^h 26 ^m 35 ^s
DEC (J2000)	–47:30:24	–47:26:49	–47:31:25	–47:27:54
ν (Hz)	52.7673968(13)	282.7492616(3)	145.2721066(14)	242.123215(7)
DM ₀ (pc cm ^{–3})	102.555	101.4759	102.1	95.923
Orbital parameters				
P_b (days)	3.508256(2)	0.1589288660(7)	6.3566263(6)	1.5400249(3)
x (ls)	0.7852(16)	0.061800(6)	5.7231(14)	1.9938(2)
T_A (MJD)	59293.4482(9)	59294.704728(4)	...	59282.38117(12)
η	$-4.6(\pm 13.2) \times 10^{-4}$	$1.0(\pm 1.9) \times 10^{-4}$...	$4.4(\pm 9.7) \times 10^{-5}$
κ	$1.6(\pm 0.9) \times 10^{-3}$	$1.5(\pm 2.0) \times 10^{-4}$...	$5.5(18.5) \times 10^{-5}$
T_0 (MJD)	59292.3196(12)	...
ω (°)	241.78(7)	...
e	0.09282(11)	...
Derived parameters				
P_s (ms)	18.9510959(5)	3.536702428(4)	6.88363392(7)	4.13012854(12)
M_c (M_\odot)	> 0.043	> 0.027	> 0.232	> 0.205

Notes. Minimum companion mass derived from the mass function and assuming a pulsar mass of $M_p = 1.35 M_\odot$ and an inclination angle of $i = 90^\circ$.

Appendix E: Chandra sources and NICER FoV

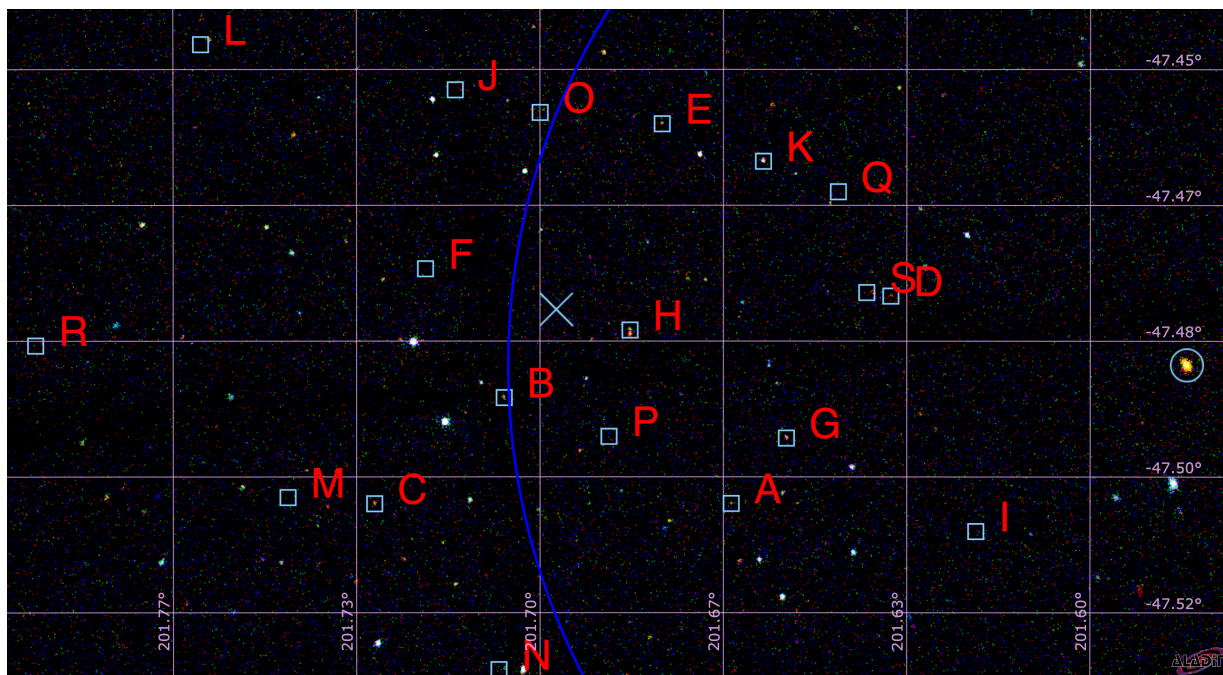


Fig. E.1: ω Cen pulsar population overlaid on a *Chandra* X-ray image (via the Aladin Sky Atlas; Baumann et al. 2022), showing several source coincidences. The cross marks the cluster centre; the large blue circle shows the NICER FoV analysed here, centred on the quiescent LMXB CXOU 132619.7–472910.8 (cyan; Rutledge et al. 2002).

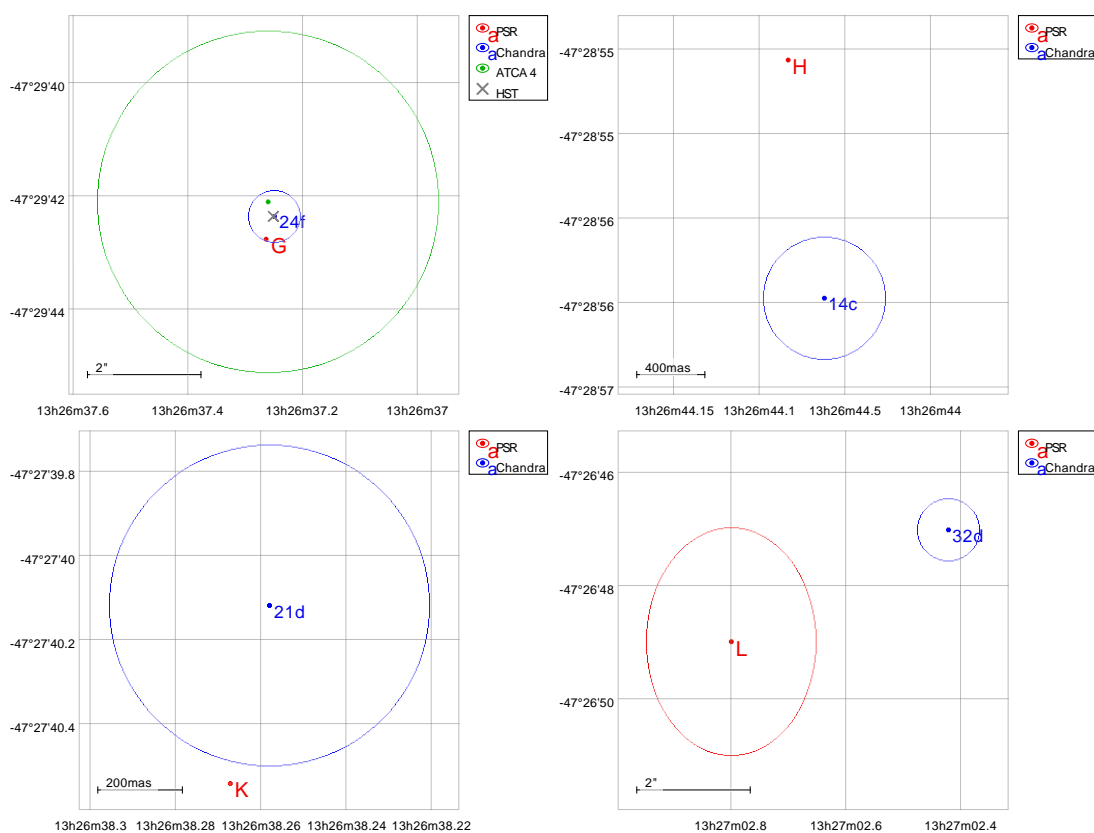


Fig. E.2: Positions of G, H, K, and L compared with their nearest *Chandra* X-ray (Henleywillis et al. 2018), ATCA (Dai et al. 2023), and HST (Cool et al. 2013) counterparts. Timing positions are used for G, H, and K; L uses the localisation from Chen et al. 2023. Drawn with TOPCAT (<http://www.starlink.ac.uk/topcat/>, Taylor 2005).